Journal of Structural Geology 140 (2020) 104119

Contents lists available at ScienceDirect

Journal of Structural Geology

journal homepage: http://www.elsevier.com/locate/jsg

Rift segment interaction in orthogonal and rotational extension experiments: Implications for the large-scale development of rift systems

Frank Zwaan *, Guido Schreurs

Institute of Geological Sciences, University of Bern, Baltzerstrasse 1+3, CH-3012, Bern, Switzerland

ARTICLE INFO

Keywords:
Rifting
Rotational extension
Rift propagation
Transfer zone
Accommodation zone
Analogue modelling

ABSTRACT

During extension of the continental lithosphere, rift basins develop. These are often initially offset, and must interact and connect in order to create a continuous rift system that may ultimately achieve break-up. When simulating extensional tectonics and rift interaction structures, analogue and numerical modellers often apply a continuous extension rate along the strike of a rift or rift system. Yet in nature significant extension velocity variations occur along rifts and plate boundaries as a natural consequence of tectonic plates moving apart about a pole of rotation, resulting in rotational extension, and associated rift propagation and structural gradients. Here we present various analogue tectonic experiments to assess rift interaction structures forming in orthogonal extension settings versus rotational extension settings. Our modelling efforts show that rotational extension and orthogonal extension produce significantly different large-scale structures. Rotational extension can cause important variations in rift maturity between rift segments, delay rift interaction zone development, and make rift segments propagate in opposite directions. Still, local features in a rotational extension system can often be regarded as evolving in an orthogonal extension setting. Furthermore, we find that various degrees of rift underlap produce three basic modes of rift linkage structures. Low underlap distance (high angle φ) experiments develop rift pass structures. With increasing underlap distance (φ = ca. 40°), transfer zone basins develop. High degrees of underlap (φ ≤ 30°) tend to result in en echelon sub-basins. Our results match with data from previous modelling efforts and natural examples. We furthermore propose a large-scale tectonic scenario for the East African Rift System based on rotational extension and associated rift propagation. These insights may also be applicable when studying other large-scale rift systems.

1. Introduction

An important feature associated with rift structures is their tendency to develop along structural inheritances such as old faults or shear zones, locally thinned lithosphere or old orogenic belts (e.g. Morley et al., 1990; Nelson et al., 1992; Dyksterhuis et al., 2007; Corti, 2012 and reference therein). As a result, initial rift basins are often poorly aligned and need to link up to form a continuous rift system, as observed in the East African Rift System (EARS) (e.g. Chorowicz, 2005; Corti, 2012, Fig. 1b) and the North Sea Rift System (e.g. Erratt et al., 1999, 2010). These rift interaction structures are classified as transfer zones when hard linkage occurs through direct fault connection, while in an accommodation zone soft linkage takes place, i.e. faults do not connect, so that deformation is distributed (Rosendahl, 1987; Larsen, 1988; Childs et al., 1995; Faulds and Varga, 1998). Rift linkage zones are important structures during rifting and continental break-up, as they may represent the predecessors of subsequent transform faults in the oceanic domain (e.g. the Labrador Sea, the South Atlantic or the Knipovich ridge in the Arctic, Fig. 1c, Bellahsen et al., 2003, Heine et al., 2013; Heron et al., 2019). In addition, linkage zones can influence the migration of melts and hydrocarbons, providing complex structural traps such as present in the Viking Graben in the North Sea and in rift and passive margin settings in general (e.g. Morley et al., 1990; Corti et al., 2004; Fossen et al., 2010; Minor et al., 2013; Paul and Mitra, 2013).

Various analogue and numerical modelling studies have investigated rift segment interaction, highlighting the importance of primary and secondary structural inheritances and their geometry, the influence of extension velocity and direction (e.g. Elmohandes, 1981; Acocella et al., 1999; Tentler and Acocella, 2010; Brune et al., 2012; Zwaan et al., 2016; Zwaan and Schreurs, 2017). However, when simulating lithospheric extension, modellers routinely apply a constant extension rate along the strike of a rift or rift system (e.g. Michon and Merle, 2000; Van Wijk and

* Corresponding author.
E-mail addresses: frank.zwaan@geo.unibe.ch, fzwaan@hotmail.com (F. Zwaan).

https://doi.org/10.1016/j.jsg.2020.104119
Received 3 March 2020; Received in revised form 5 June 2020; Accepted 8 June 2020
Available online 18 June 2020

Blackman, 2005; Le Pourhiet et al., 2018). This is true for models of both orthogonal and oblique extension, where the direction of extension is at an angle with respect to the rift trend (e.g. McClay and White, 1995; Van Wijk, 2005; Philippon et al., 2015). Also in models involving changing extension obliquities along strike, the extension velocity is generally kept constant (e.g. Corti et al., 2007).

Yet in nature, we often observe significant extension velocity gradients along the strike of diverging plates, as the natural consequence of these plates rotating about a rotation pole (e.g. Martin, 1984; Van der Pluijm and Marshak, 2004), resulting in V-shaped oceanic basins and rifts. Such extension gradients exist for instance in the Red Sea and the Gulf of Aden oceanic basins (Fig. 1a), caused by the anticlockwise rotation of the Arabian peninsula (Bellahsen et al., 2003; Bosworth et al., 2005; ArRajehi et al., 2010). Other examples may be found along the East African Rift System (EARS), which contains several branches with changing extension rates (Saria et al., 2014, Fig. 1b), and in the Arctic,

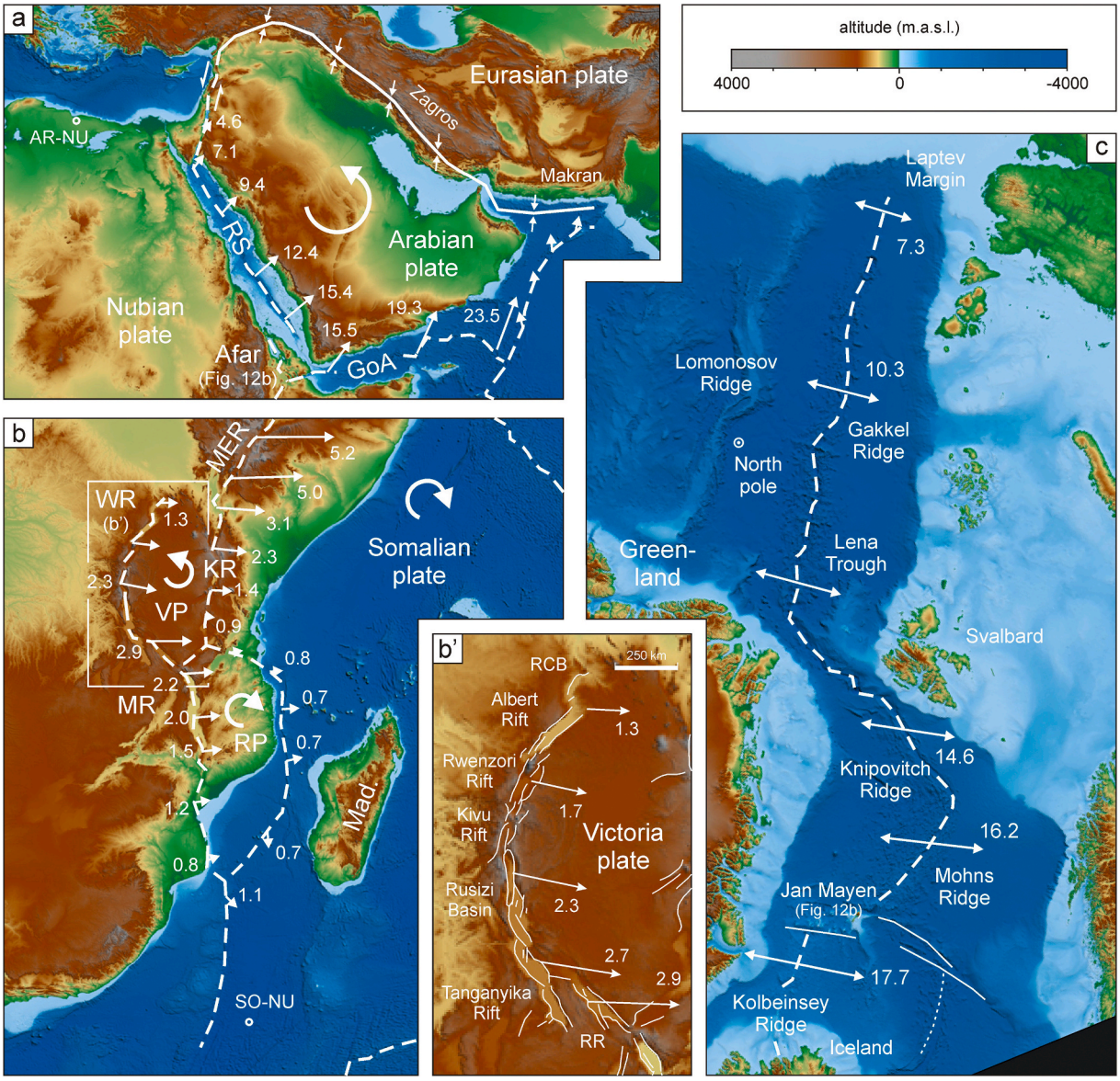

Fig. 1. Natural examples of extension gradients and rift interaction structures. (a) The anticlockwise block rotation of the Arabian plate about a rotation pole in Egypt (AR-NU: Arabia-Nubia pole of rotation) causes increasing extension rates in the Red Sea (RS) and the Gulf of Aden (GoA) oceanic basins. Image modified after Bellahsen et al. (2003), Bosworth et al. (2005), ArRajehi et al. (ArRajehi et al., 2010), Deprez et al. (2013) and Saria et al. (2014). (b) Southward from the Afar triple junction, extension rates decrease along the rift segments of the East African Rift System (EARS), e.g. the Main Ethiopian Rift (MER), due to general clockwise rotation of the Somalian plate about a pole SE of South Africa (SO-NU: Somalia-Nubia pole of rotation). Note how the western and eastern branches of the EARS (i.e. the Western Rift [WR, Purcell, 2017], and the Kenya Rift [KR] and MER, respectively) form overlapping rift segments (rift pass) around the Tanzanian craton or Victoria plate (VP), causing it to rotate counterclockwise (Glerum et al., 2020). More to the south, extension decreases along the Malawi Rift (MR), and part of the extension is accommodated by clockwise rotation of the Rovuma plate (RP). Image modified after Deprez et al. (2013) and Saria et al. (2014). (b') zoom in of Western Rift branch of the EARS, depicting its various rift segments and rift interaction structures. RCB: Rhino-Camp Basin, RR: Rukwa Rift. Modified after Ebinger et al. (1989), Acocella et al. (1999), Abeinomugisha and Njabire (2012), Corti (2012) and Saria et al. (2014). For location, see (b). (c) Artic region, showing an increasing extension velocity along the Gakkel Ridge towards the North Atlantic, with large-scale transfer zone structures at the Knipovitch Ridge and overlapping spreading centers at the Jan Mayen microcontinent. Image modified after Dick et al. (2003) and Jakobsson et al. (2012). Arrows indicate extension directions and velocities (in mm/yr), in (a–b) with respect to a fixed Nubian plate, in (c) with respect to the central mid-oceanic ridge. Note that vector scale changes between (a–c). Background topography and bathymetry is derived from GEBCO (2020) and the IBCAO maps (Jakobsson et al., 2012). (For interpretation of the references to colour in this figure legend, the reader is referred to the Web version of this article.)

where the Gakkel Ridge displays an increasing extension velocity towards the North Atlantic (Dick et al., 2003, Fig. 1c).

The few (analogue) modelling studies that incorporate such extension gradients focus on oceanic transform fault formation (O'Bryan et al., 1975), or the transition from a localized ridge into deformation-dissipating continental crust found at the Laptev Margin (Fig. 1c) and in the Taupo Rift of New Zealand (Benes and Scott, 1996). Other studies investigate subduction rollback causing back-arc extension, for instance in the Pacific Kuril Basin (Schellart et al., 2002, 2003) and the Aegean (Kydonakis et al., 2015) or the development of the South China Sea (Sun et al., 2009). Recent work by Molnar et al. (2017, 2018) assesses the influence of large-scale lithospheric weaknesses on rift propagation in the Red Sea. Furthermore, Molnar et al. (2019) explore the effects of (multiple) obliquely oriented crustal weaknesses in similar systems. Finally, Mondy et al. (2018) and Zwaan et al. (2020) clearly illustrate how rift propagation in rotational extension settings is distinctly different from the orthogonal extension equivalent; the latter creates rift basins with very constant features along-strike, whereas the former leads to the development of structural gradients and rift propagation, including along-axial displacement of material, thus highlighting the 3D aspects of rifting.

Here we build on these previous works and present a modelling study exploring the differences in rift linkage structure development between orthogonal extension settings (i.e. constant extension velocity along strike) and rotational extension settings (i.e. extension velocity gradient along strike). Our modelling technique involves a distributed type of deformation, allowing a high degree of freedom for rifts and rift interaction structures to develop. X-ray computed tomography (XRCT or CT) techniques are used for the analysis of selected models, providing unique insights into their 3D internal evolution. We subsequently compare our experimental results with previous modelling studies and natural examples of rift interaction structures, and develop scenario for the large-scale evolution of the EARS involving rotational extension.

2. Materials and methods

2.1. Material properties

Both brittle and viscous materials are applied in our models, representing the brittle and ductile parts of the continental crust, respectively, but could also serve to simulate an oceanic setting (see section 2.3). The 20 km brittle upper crust is modelled by a 4 cm thick layer of fine quartz sand (ø = 60–250 μm), sieved from ca. 30 cm height into the experimental apparatus, ensuring a constant sand density of ca. 1560 kg/m^3 (Zwaan et al., 2018b; Schmid et al., 2019). We also flatten the sand using a scraper at every cm during the build-up of the model, to create slight density differences. This "layering" subsequently appears on CT images (Fig. 6).

We apply a 4 cm thick viscous layer to simulate a 20 km thick lower crust. The viscous material is a mixture of SGM-36 polydimethylsiloxane (PDMS) and dense corundum sand following a 0.965 : 1.00 weight ratio, and has a near-Newtonian rheology (η = ca. 1.5·10^5 Pa·s; n = 1.05–1.10, Zwaan et al., 2018c). The density of this viscous mixture is c. 1600 kg/m^3 and slightly higher than the overlying quartz sand, yielding a vertical density profile that is closer to the natural situation than when using pure PDMS ($\rho_{specific}$ = ca. 965 kg/m^3), thus preventing unrealistic buoyancy effects. Further material properties are presented in Table 1.

2.2. Experimental set-up

We use two different machines with the same basic method to induce deformation, involving an 8 cm thick RG 50 Polyurethane foam block compressed between two longitudinal sidewalls. The model materials are subsequently applied on top of the foam base (Fig. 2a, c). During a model run, precise computer-controlled motors drive the sidewalls apart. Consequently, the foam expands uniformly, causing distributed extension that is transferred to the overlying model materials. It may be noted that although our brittle-viscous set-ups include complex viscous flow (Zwaan et al., 2018a, Zwaan et al., 2020), the models lack direct asthenospheric influences (isostatic compensation and asthenospheric flow as observed by Koopmann et al., 2014; Mondy et al., 2018).

Table 1
Material properties.

Granular materials	Quartz sand[a]	Corundum sand[b]
Grain size range	60–250 μm	88–125 μm
Density (specific)[c]	2650 kg/m^3	3950 kg/m^3
Density (sieved from 30 cm high)	1560 kg/m^3	1890 kg/m^3
Angle of internal peak friction	36.1°	37°
Angle of dynamic-stable friction	31.4°	32°
Cohesion	9 ± 98 Pa	39 ± 10 Pa
Viscous materials	Pure PDMS[a, d]	PDMS/corundum sand mixture[a]
Weight ratio PDMS: corundum sand	0.965 kg: 1.00 kg	
Density	965 kg/m^3	ca. 1600 kg/m^3
Viscosity	ca. 2.8·10^4 Pa·s	ca. 1.5·10^5 Pa·s[e]
Viscous flow type[f]	Newtonian (n = ca. 1)	near-Newtonian (n = 1.05–1.10)

[a] Quartz sand, PDMS and viscous mixture characteristics after Zwaan et al. (2016, 2018b,c).
[b] Corundum sand characteristics after Panien et al. (2006).
[c] Specific densities after Carlo AG (2020)
[d] Pure PDMS rheology after Rudolf et al. (2016)
[e] Viscosity value holds for model strain rates < 10^{-4}/s.
[f] Power-law exponent n (dimensionless) represents sensitivity to strain rate.

The main difference between both set-ups lies within the sidewall motion. In the orthogonal extension set-up (O-series, Fig. 2a, c, c'), the sidewalls move apart in a perpendicular fashion, producing uniform extension velocity along strike applied in most rifting model studies. For the rotational tectonic setting, however, the sidewalls pivot about a vertical axis that divides the model in a 65 cm long extensional sector and a 25 cm long compressional sector (R-series, Fig. 2b, d, d'). We ignore the structures developing in the compressional domain for this study; although previous work has shown viscous flow along the strike of the rift, part of which may be due to loading due to compression, this seems to have little influence on large-scale structures in the extensional domain (Zwaan et al., 2020). Both sectors develop a deformation gradient away from the rotation axis, where no faulting takes place. The far ends of the extensional sector in the rotational extension set-up move with the same velocity as the sidewalls in the orthogonal extension set-up, i.e. 4 mm/h per sidewall for a total of 8 mm/h, whereas extension is zero at the rotation axis.

In order to contain the model materials and to diminish boundary effects, we use either rubber or curved foam sidewalls at the short ends of the models (Fig. 2a and b). These uniformly deforming materials decrease boundary effects at the model edges while the curvature of the foam is necessary to allow for a smooth pivoting of the sidewalls in the rotational extension set-up (Fig. 2b). A 4 × 4 cm grid on the model surface yields a first-order impression of surface deformation. Furthermore, every component of the machine around the experiment consists of X-ray transparent materials to allow for CT-scanning, revealing 3D internal model evolution (Fig. 2g).

Thin rods (1 cm thick, semi-cylindrical "seeds") of the viscous PDMS/corundum sand mixture on top of the basal viscous layer (Fig. 2a, b, e, f), act as linear weak zones and represent discrete linear crustal weaknesses since the strong sand cover is locally thinner and thus weaker above the seeds, causing deformation to localize (e.g. Le Calvez and Vendeville, 2002; Zwaan and Schreurs, 2017, Molnar et al., 2017, Fig. 2f). Seed offset is set to 8 cm for all models (Fig. 2f), equivalent to twice the brittle layer thickness H (i.e. 4 cm for this analogue modelling study), in order

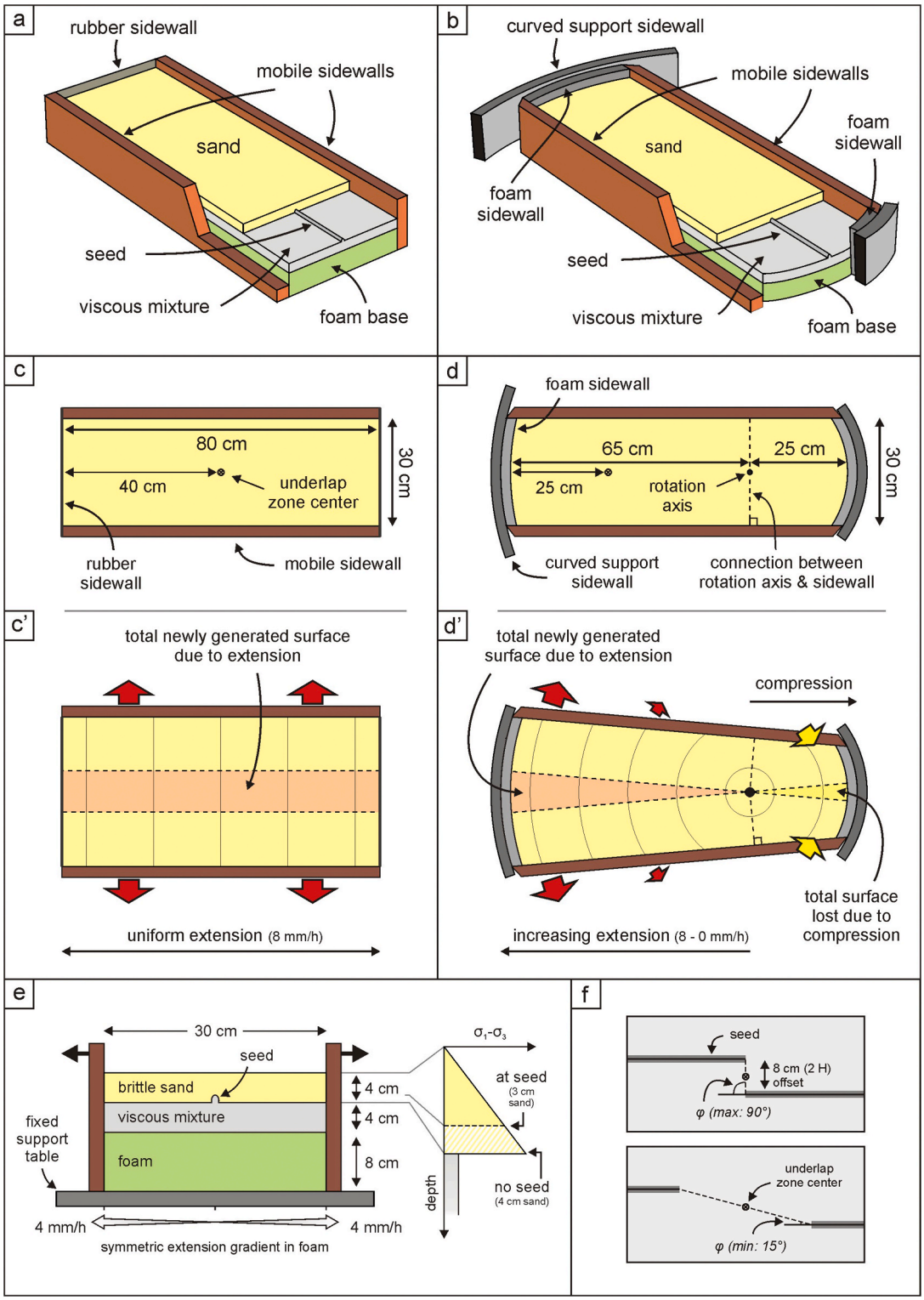

Fig. 2. Model set-up. (a–b) Cut-out views of the orthogonal extension apparatus (a) and rotational extension apparatus (b), depicting their various components. (c-c') Top view illustration of our orthogonal extension set-up. (d-d') Top view depiction of our rotational tectonic set-up. A connection at the base of the model (dotted line) allows the sidewalls to pivot around the rotation axis, inducing extension or shortening on either side of the axis. Extension is exaggerated in panels (c') and (d') in order to expose the differences between both set-ups. (e) Left: schematic section through the extensional sector of our experiments showing the foam base and the extension gradient that develops when the sidewalls are moving apart, as well as the fixed table that supports the foam itself. On top of the foam base the brittle-viscous layers including the seed(s) are applied, which deform as the sidewalls move apart and the foam expands. Right: schematic strength profile, showing the differences in strength of the brittle layer above and away from the seed. In the latter case the brittle layer is 56% weaker since sand thickness is reduced by 25% (Zwaan et al., 2020). (f) Seed geometry definition. Angle φ is the angle between seed strike and the horizontal line connecting the two seed tips, which ranges between 90° and 15° in this paper.

Table 2
Model parameters.

	Model	Seed (angle φ)	Shown in*		Model	Seed (angle φ)	Shown in*
Orthogonal extension models	O1	90°	Figs. 3, 4 and 7	**Rotational extension models**	R1	90°	Fig. 3
	O2	90°	–		R2	90°	–
	O3	60°	Fig. 3		R3	60°	Fig. 3
	O4	50°	Figs. 3 and 4		R4	50°	Fig. 3
	O5	45°	Fig. 3		R5	45°	Fig. 3
	O6	40°	–		R6	45°	–
	O7	40°	Figs. 3 and 7		R7	40°	Fig. 3
	O8	30°	Fig. A1		R8	30°	Fig. 3 and B1
	O9#	30°	Figs. 3–6 and A1		R9	30°	Fig. B1
	O10	30°	Fig. A1		R10#	30°	–
	O11	20°	Figs. 3 and 7		R11[a]	30°	–
	O12	15°	Fig. 3		R12[b]	30°	–
					R13[c]	30°	Fig. B1
					R14	20°	–
					R15#	20°	–
					R16	20°	Figs. 3 and 4
					R17	15°	Fig. 3

CT-scanned model.
* Model results not shown in this paper are available in the supplementary material (Zwaan and Schreurs, 2020).
[a] Overlap zone center 5 cm to the left.
[b] Overlap zone center 5 cm to the right.
[c] Thicker seed test.

to avoid rift proximity effects (Zwaan et al., 2016). Various degrees of seed underlap (measured by angle φ, Zwaan and Schreurs, 2017, Fig. 2f) are tested in the experiments. The center of the underlap zone was put at 40 cm from the rotation axis in the rotational experiments, and at the centre of the model for orthogonal extension experiments (Fig. 2c, d, f). This fixed rotation pole in our set-up is a simplification, since the Euler pole of a rotational rift system can wander over geological history (e.g. Torsvik et al., 2012; DeMets and Merkouriev, 2016; Brune, 2018). Yet these variations are often minor and the pole mostly remains in the extension of the rift axis, so that the extension gradient remains very similar. Therefore our relatively simple rotational extension models should provide good insights into rift development under such conditions.

The duration of every model run is 5 h, amounting to 40 mm of total (maximum) extension. Top view time-lapse photography captures surface evolution. Additional CT-scanning of selected experiments was done at 30 min intervals (i.e. every 4 mm of extension), which yields a detailed 4D record of internal model evolution. Furthermore, top view images taken after removal of the sand layer reveal the deformation of the viscous layer at the end of the experiments. We do not implement syn-rift sedimentation in our models, which is permissible for a first-order structural analysis (Zwaan et al., 2018a). We completed 29 experiments in total, the details of which are summarized in Table 2.

2.3. Model scaling

In order to correctly scale our models we compute stress ratios (σ*, convention: $\sigma^* = \sigma_{model}/\sigma_{nature}$) using the following equation (Hubbert, 1937; Ramberg, 1981): $\sigma^* = \rho^* \cdot h^* \cdot g^*$, where ρ*, h* and g* represent the density, length and gravity ratios respectively. We derive the strain rate ratio $\dot{\varepsilon}^*$ by means of the aforementioned stress ratio σ* and the viscosity ratio η* (Weijermars and Schmeling, 1986): $\dot{\varepsilon}^* = \sigma^*/\eta^*$. Subsequently, the velocity ratio v* and time ratio t* can be acquired through the following equations: $\dot{\varepsilon}^* = v^*/h^* = 1/t^*$. We assume an intermediate viscosity for the lower crust ($\eta = 10^{21}$, Buck, 1991), so that 1 h in our experiment translates to 0.84 Ma in nature. Consequently, our experimental extension velocity of 8 mm/h scales up to ca. 5 mm/y, which is very similar to typical natural extension velocities for continental rifts (several mm/y, e.g. Saria et al., 2014, Fig. 1b). All scaling parameters are listed in Table 3.

Dynamic similarity between our brittle model materials and their counterparts in the upper crust can de demonstrated by means of ratio Rs,

Table 3
Scaling parameters.

		Model	Nature (continent)	Nature (ocean)
General parameters	Gravitational acceleration (g)	9.81 m/s^2	9.81 m/s^2	9.81 m/s^2
	Extension velocity (v)	$2.2 \cdot 10^{-6}$ m/s	$1.5 \cdot 10^{-10}$ m/s	$3.7 \cdot 10^{-10}$ m/s
	Length	0.8 m*	$4 \cdot 10^5$ m	$1.4 \cdot 10^5$ m
	Width	0.3 m	$1.5 \cdot 10^5$ m	$5.3 \cdot 10^4$ m
Brittle layer	Material/represents	Sand layer	Upper crust	Oceanic crust
	Thickness (h)	$4 \cdot 10^{-2}$ m	$2 \cdot 10^4$ m	$7 \cdot 10^3$ m
	Density (ρ)	$1.56 \cdot 10^3$ kg/m^3	$2.8 \cdot 10^3$ kg/m^3	$3.0 \cdot 10^3$ kg/m^3
	Cohesion (C)	9 Pa	$8 \cdot 10^6$ Pa	$3 \cdot 10^6$ Pa
Viscous/ductile layer	Material/represents	PDMS/cor. sand mix	Lower crust	(upper part of the) Lithosph. mantle
	Thickness (h)	$4 \cdot 10^{-2}$ m	$2 \cdot 10^4$ m	$7 \cdot 10^3$ m**
	Density (ρ)	$1.6 \cdot 10^3$ kg/m^3	$2.87 \cdot 10^3$ kg/m^3	$3.01 \cdot 10^3$ kg/m^3
	Viscosity (η)	$1.5 \cdot 10^5$ Pa·s	$1 \cdot 10^{21}$ Pa·s	$5 \cdot 10^{19}$ Pa·s
Dynamic scaling values	Brittle stress ratio (R_s)	68	69	69
	Ramberg number (R_m)	75	75	81

* for the orthogonal extension models, the rotational extension models are 0.9 m long.
** only the upper part of the lithospheric mantle is represented in the experiments.

(Ramberg, 1981; Mulugeta, 1988): R_s = gravitational forces/cohesion = $(\rho \cdot g \cdot h)/C$. In the case of viscous materials, we apply the Ramberg number R_m (Weijermars and Schmeling, 1986): R_m = gravitational forces/viscous forces = $(\rho \cdot g \cdot h^2)/(\eta \cdot v)$. An upper crustal cohesion of 8 MPa yields almost the same R_s value as the model equivalent (i.e. 69 vs. 68). Although this natural cohesion value is slightly below those reported by experimental rock deformation studies (e.g. Handin, 1969; Jaeger and Cook, 1976; Twiss and Moore, 1992), we consider it quite acceptable since the lithosphere as a whole is often weakened by preceding deformation phases. Furthermore, both the model and natural parameters yield the same Ramberg number: 75. We therefore regard our models as appropriately scaled for studying continental rifting. Furthermore, as described by Zwaan et al. (2020), our set-ups are also suitable for simulating oceanic systems when assuming a 7 km thick brittle oceanic crust overlying a ductile lithospheric mantle (Table 3).

3. Model results

3.1. Overview of final model results

We present a selection of the final model results in an overview figure (Fig. 3), which depicts the various structures that develop under orthogonal extension and rotational extension conditions (Fig. 3a and b, respectively).

In the orthogonal extension set-up (Fig. 3a), rift basins form above the initial seeds in all experiments. For models with underlap angle φ down to 45°, rifts propagate laterally, roughly parallel to the trend of the underlying seed, with a tendency to deviate towards the other rift segment in the area where no seed is present. In most cases, one of the rift branches is dominant and can (almost) reach the other rift branch (e.g. φ = 50°, Model O4 in Fig. 3a). Only in the φ = 90° case (Model O1,

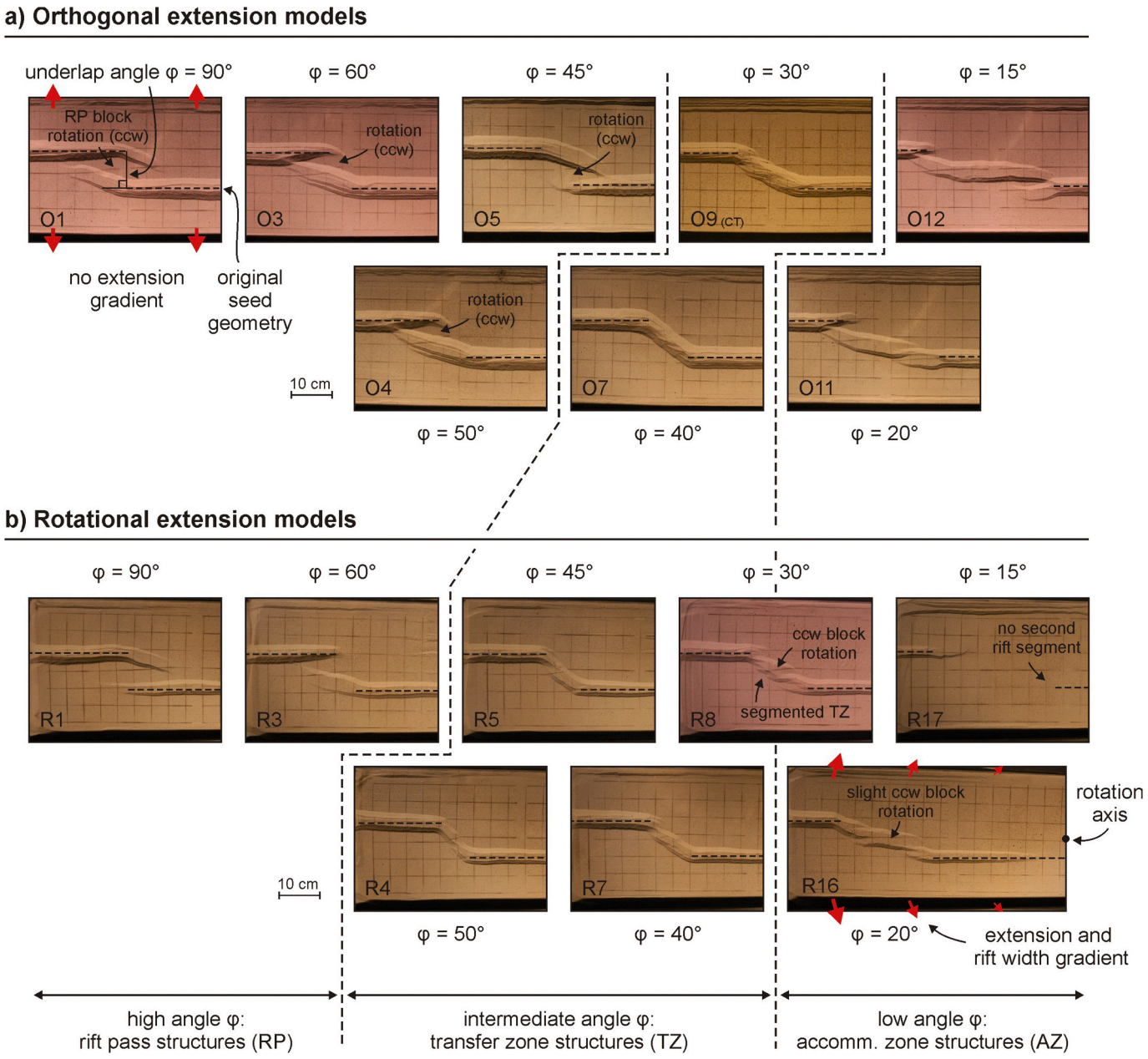

Fig. 3. Final surface structure overview of representative model results from both (a) the orthogonal extension models and (b) the rotational extension models as a function of rift underlap (angle φ). The three types of rift interaction structure (rift pass [RP], transfer zone [TZ] or accommodation zones [AZ] with en echelon basins) are indicated. Note that the images are cropped (focussing on zone around the underlap centre, see Fig. 2c, d, f). Only rotational extension model Model R16 shows the full extent of the extensional domain. ccw: counterclockwise. Dashed black lines indicate the initial position of the viscous seeds underlying the sand cover.

Fig. 3a), both rifts are propagating equally, creating a so-called "rift pass" structure (Nelson et al., 1992) or "overlapping spreading center" configuration when situated in an oceanic domain (Hieronymus, 2004). This involves slight counterclockwise rotation of the block between both rift branches as indicated by the deformed surface grid (Model O1 in Fig. 3a). Similar rotation of the blocks caught between overlapping rift segments occur in all orthogonal extension models with $90° \geq \varphi \geq 45°$ (Fig. 3a).

However, the $\varphi \leq 40°$ experiments (Models O7 and O9 in Fig. 3a) mark a distinct change in structural style. In these models, the main rift

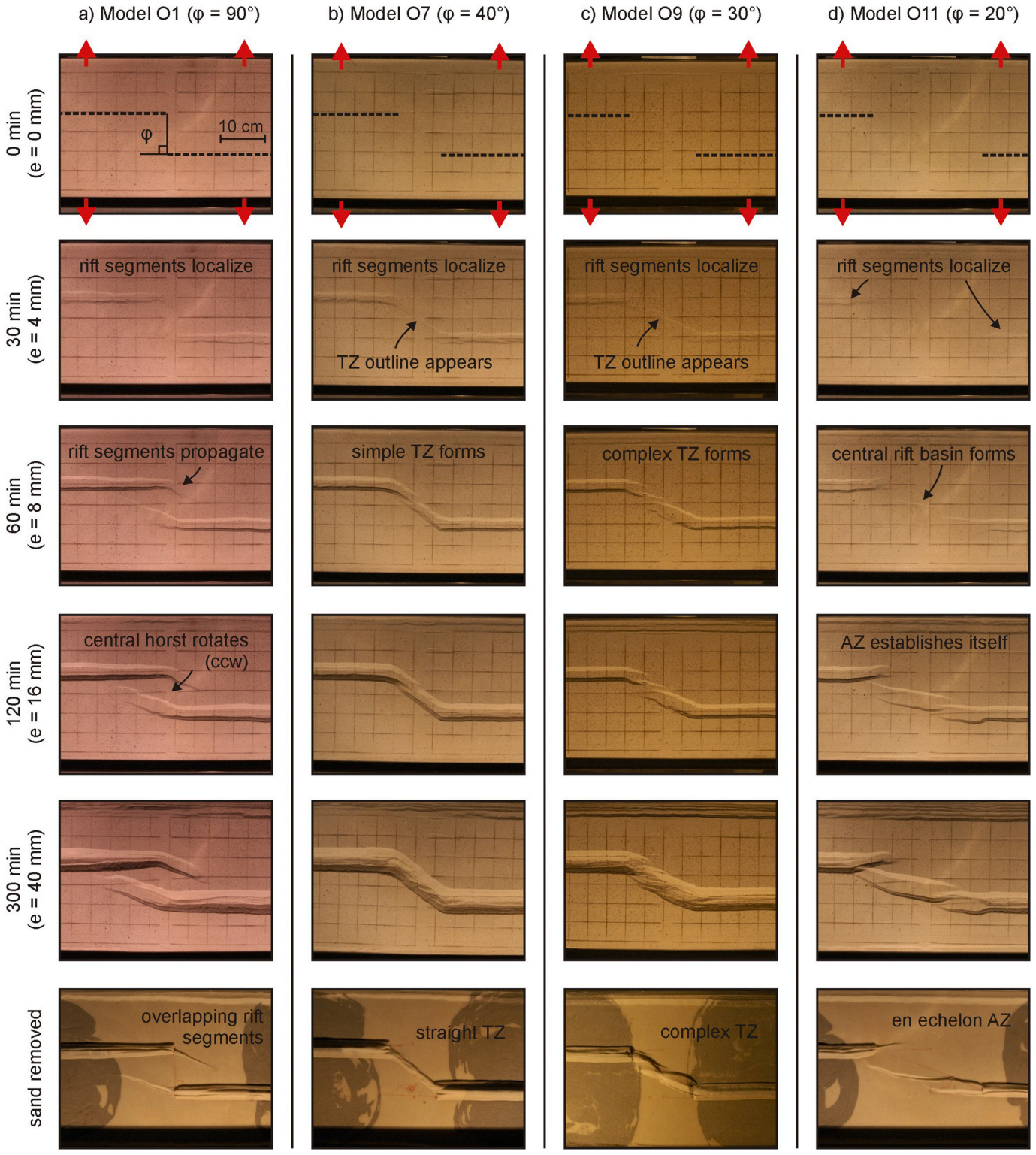

Fig. 4. Surface evolution of representative orthogonal extension models depicting the various types of rift interaction structures (rift pass [RP], transfer zone [TZ] and accommodation zone [AZ]). Colour differences in the top views without sand cover (bottom row) are due to differently coloured corundum sand used for the viscous mixture and have no influence on the material's rheology. ccw: counterclockwise. (For interpretation of the references to colour in this figure legend, the reader is referred to the Web version of this article.)

segments grow directly into each other and connect through a transfer zone, resulting in continuous rift boundary faults. Note that these two experiments also develop minor oblique rift-internal faults that are sub-parallel with respect to the rift segment orientation. When the rift underlap distance increases even further (i.e., decreasing angle φ down to 15°), these oblique structures become dominant (Models O11 and O12 in Fig. 3a); instead of a transfer zone, these models develop en echelon rift basins between the main rift segments. The larger the underlap distance, the larger this intermediary basin. Some block rotation is involved as well, best visible in the φ = 20° case (Model O11 in Fig. 3a).

When rotational extension is applied, the results are quite similar to those of the orthogonal extension experiment (Fig. 3b). Also here, we observe propagating rift segments when angle φ is high (Model R1 and R3 in Fig. 3b). However, the transition from rift pass geometries to a continuous transfer zone structure occurs a bit earlier than in the orthogonal extension models, with φ = 50° and continues to φ = 40° (Models R4 and model R7 in Fig. 3b, respectively). When angle φ

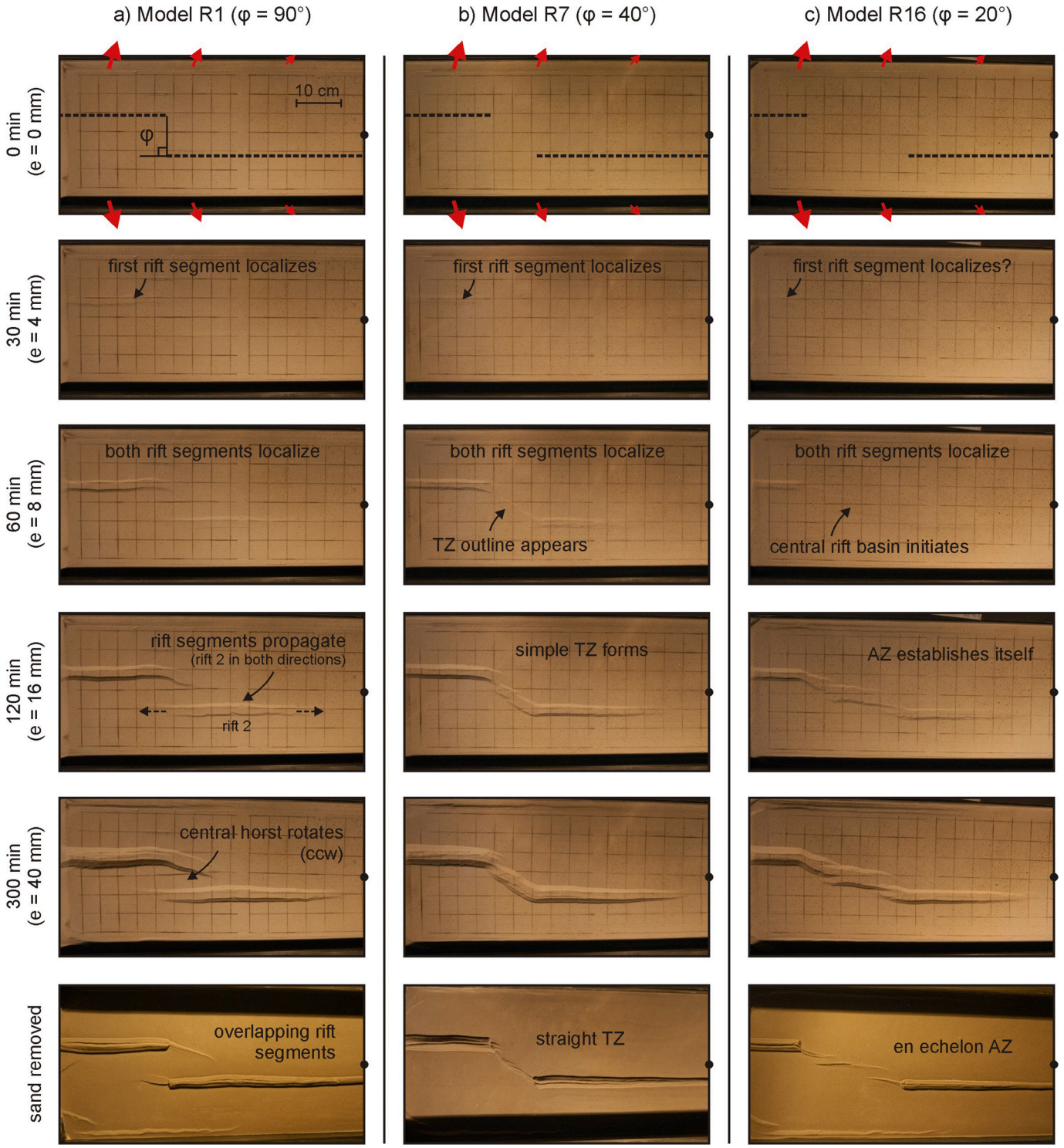

Fig. 5. Surface evolution of representative rotational extension models depicting the various types of rift interaction structures: rift pass [RP], transfer zone [TZ] and accommodation zone [AZ]). ccw: counterclockwise.

decreases to 30° (Model R8 in Fig. 3b), the transfer zone becomes segmented, indicating a shift to the accommodation zone mode. With φ = 20° (Model R16 in Fig. 3b) a full intermediary basin develops. In both cases, the system develops slight block rotation within the accommodation zone (Fig. 3b). In our φ = 15° model (Model R17 in Fig. 3b), no second rift segment develops as the seed does not localize deformation (see also Appendix B), but would otherwise likely create a similar accommodation zone as in Model O12 (Fig. 3a).

A significant difference with the orthogonal extension models is the width of the rift segments. In the orthogonal extension models, the final rift width along the main rift segments amounts to ca. 4.7 cm (Fig. 3a). In the rotational extension experiments however, rift width is largest to the left (4.5 cm), where most extension is concentrated and narrowest towards the rotation axis to the right, where total extension is limited to absent (best visible in the uncropped top view of Model R16 in Fig. 3b).

3.2. Model evolution

We thus find three main types of rift interaction structures (overlapping rifts, transfer zones or accommodation zones with en echelon rift basins, Fig. 3) that develop as a factor of rift underlap in both orthogonal and rotational extension models. We present a comparison of the general surface structure evolution of these three rift interaction modes by means of selected models (Fig. 4).

In orthogonal extension models, rift segments have clearly localized along the initial seeds after 30 min, although these structures are somewhat faint in Model O11 (Fig. 4). At this early stage, the transfer zone models (Models O7 and O9, Fig. 4b and c) already show the outline of the developing transfer zone. By contrast, the surface between the rift segments in Model O1 and O11 remains unaffected (Fig. 4a, d). After 60 min of extension, all orthogonal extension models have clearly developed their respective rift interaction structure. The early transfer zones are now well-established in Models O7 and O9 (Fig. 4b and c), the rift segments in Model O1 have started propagating to create a rift pass, and in Model O11 the central rift basin of the accommodation zone is forming. The templates for the final structure are thus created early on during model evolution (Fig. 4). Continued extension causes these structures to become more prominent, and in the case of Model O1, the propagating overlapping rift segments induce a counterclockwise rotation of the central horst block (Fig. 4a).

Removing the sand allows an examination of the deformation at the brittle-viscous interface (Fig. 4, bottom row). Below the rifts and rift interaction structures, viscous material has moved upward to isostatically compensate for the reduced load of the thinning brittle overburden (e.g. Zwaan et al., 2018a). These ridges indicate the general trends of model surface structures and we find highly distinct signatures for the three rift interaction modes (Fig. 4, bottom row). However, the brittle-vicous interface of Model O9, which forms a continuous transfer zone at the surface, reveals additional complexity (Fig. 4c). The en echelon features suggest that Model O9 represents a transition between the transfer zone and the accommodation zone mode (Fig. 4c). This interpretation is supported by the varying results when repeating the φ = 30° models (see Appendix A).

Rotational extension models show the same general structures as the orthogonal extension models (Figs. 3 and 4), yet their evolution shows important differences (Fig. 5). In contrast to the orthogonal extension models, rift development at t = 30 min only occurs along the seed farthest away from the rotation axis, where total extension is largest (Fig. 5). The second seed only localizes deformation after 60 min of extension (Fig. 5). Model R7 establishes its transfer zone early on, similarly (although slightly delayed) with respect to its orthogonal extension counterparts (Models O7 and O9, Fig. 4b and c, 5c). At the same point in time, Model R16 shows the first signs of the central rift basin within its accommodation zone. From t = 120 min on, the sequence is very similar to that of the orthogonal extension models, as the general structures of each rift interaction mode are well-established and continue to evolve, which is clearly illustrated by the structures at the brittle-viscous interface as well (Fig. 5a–c, bottom row). Yet a significant difference, next to the delayed development of the rift interaction structures, is the general positive trend in rift maturity when moving away from the rotational axis (Fig. 5a–c). As a result, the second rift in Model R1 does not only propagate towards the rotation axis, but also away from it to form the rift pass structure (Fig. 5a).

3.3. 3D CT analysis

Detailed analysis has shown that Model O9 (φ = 30°, orthogonal extension) might represent a transition between transfer zone mode and accommodation zone mode (Fig. 4c). Horizontal and vertical CT sections of this experiment provide more insights into the structural evolution of its rift linkage structures (Fig. 6). Early after model initiation (t = 30 min), simple symmetric rifts develop above the seeds and start propagating towards each other (Figs. 4c and 6b). These two rift branches do not directly link, but grow past each other, while one of them (propagating from seed 2) develops a small-scale en echelon sub-basinthat is well visible on horizontal CT sections (Figs. 4c, 6c). As deformation progresses and rift-internal structures grow more complex, the barriers between these rift arms dwindle and a continuous transfer zone basin develops at the model surface (Figs. 4c and 6d, i). Yet the internal structures at depth, however complex, remain separated until the end of the model run (Fig. 6f, j).

4. Discussion

4.1. Large-scale rift interaction structures and rift localization

Although orthogonal extension models and rotational extension models show large-scale differences in along-strike rift development (Mondy et al., 2018; Zwaan et al., 2020, Figs. 3–5), we find that both model set-ups develop a very similar sequence of rift linkage structures, which are in this study strongly depending on the degree of underlap. This can be explained by the fact that even in our rotational extension experiments, the extension direction is always approximately perpendicular to the seeds (Fig. 2c', d'). Yet the changes in extension magnitude along-strike make that rift structures form generally later when closer to the rotation pole, as also seen in the rotational models by Molnar et al. (2017), Mondy et al. (2018) and Zwaan et al. (2020), and are less developed than their orthogonal extension counterparts (Figs. 3–5). These slight differences in extension boundary conditions may have important consequences for the development of rift interaction structures in large-scale natural rift systems (see section 4.3.2).

On a more local scale, our models also show a degree of structural variability so that a certain underlap angle is not always tied to a specific rift interaction mode (Figs. 3–6 and A1). This variation is most likely the result of the foam base set-ups we use, so that our experiments are relatively free to develop compared to for instance set-ups involving moving base plates and associated velocity discontinuities (e.g. Acocella et al., 1999; Dauteuil et al., 2002). Therefore, the slightly deviant structures we observe in some models likely originate from small differences in sand, viscous layer or seed thickness, sand compaction, and other minor variations (see also section 4.2). Yet the fact that our experiments produce a logical sequence of rift interaction structures from rift pass to transfer zone to accommodation zone (Figs. 3, 4, 7a-c), illustrates the general robustness of this study's results.

4.2. Rift interaction zones and comparison with previous modelling studies

We find that the degree of initial seed underlap has a significant influence on rift linkage structures. The rift pass structures typical for our φ ≳ 45° models (Figs. 3–5, 7a) are similar to the features described by e.g. Acocella et al. (1999), Le Calvez and Vendeville (2002) and

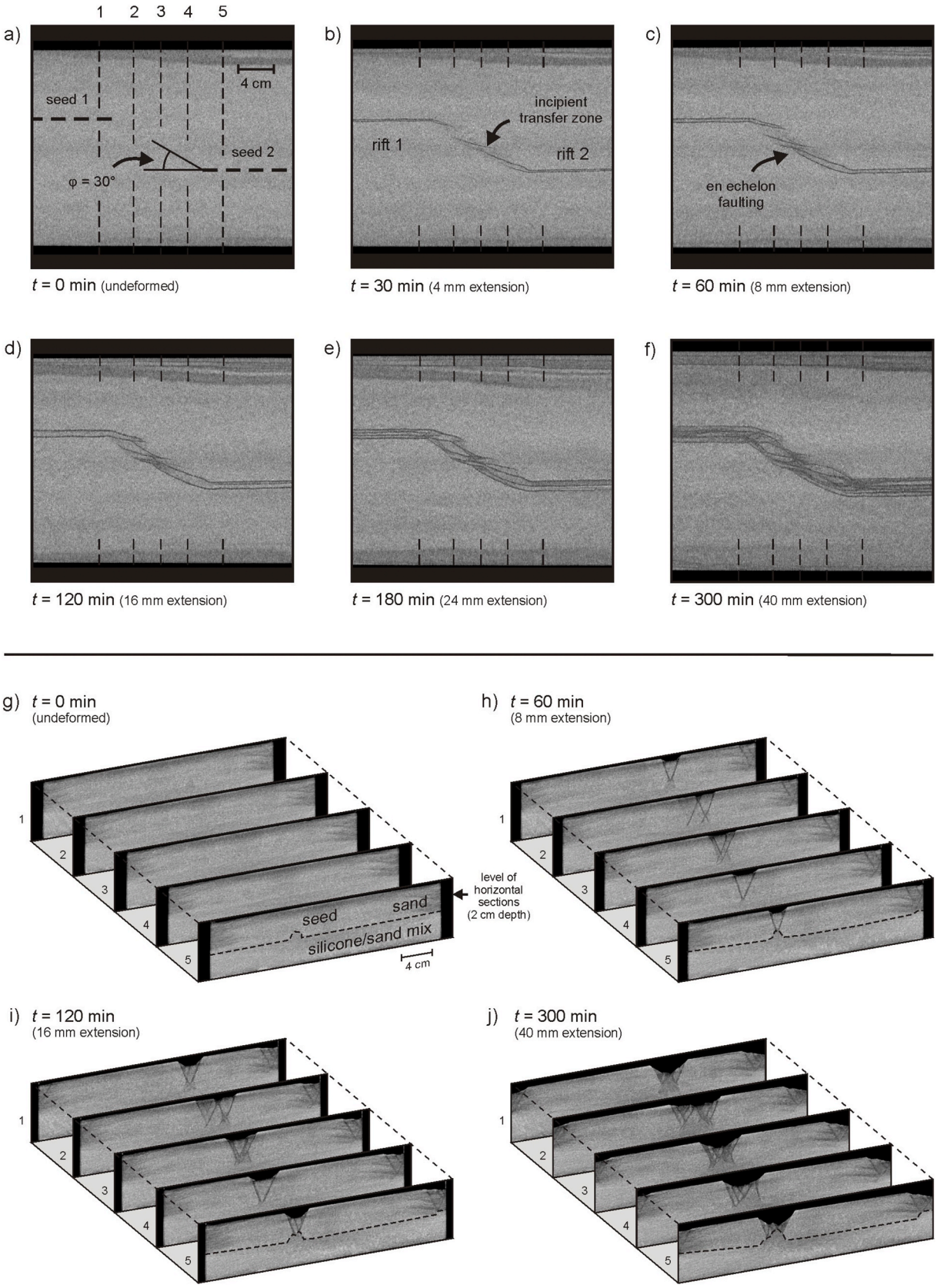

Fig. 6. CT imagery revealing the internal evolution of Model O9 (orthogonal extension, $\varphi = 30°$). (a–f) Horizontal CT section through the middle of the sand layer (2 cm depth), revealing detailed internal fault evolution in map view. (g–j) Serial vertical CT sections providing a 3D insight in model-internal evolution.

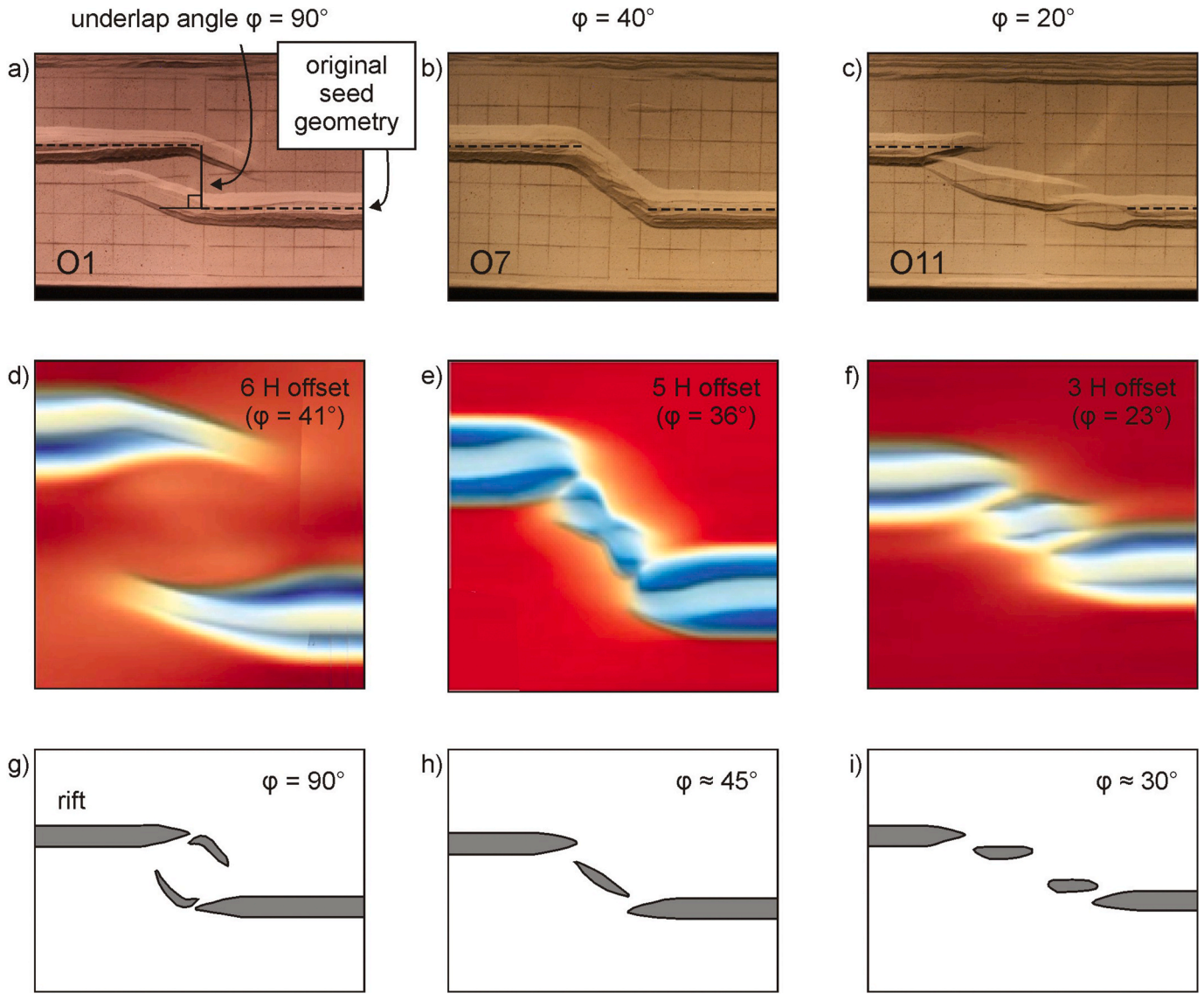

Fig. 7. Comparison with other models (a–c) Top views of our orthogonal extension models O1, O7 and O11 with 2 H offset and φ = 90°, 40° and 20°, respectively. (d–f) Top views of numerical simulations by Allken et al. (2011), with φ = 41°, 36° and 23°, and 6 H, 5 H and 3 H offset, respectively. Red indicates high areas and blue low areas. (g–i). Top view interpretations of analogue models by Tentler and Acocella (2010) with φ = 90°, 45° and 30°, respectively. Here the offset (measured in H, i.e. thickness of the brittle layer) is not clearly defined since the authors do not specify a brittle layer thickness. Panels (d–i) are reproduced with permission from John Wiley and Sons. (For interpretation of the references to colour in this figure legend, the reader is referred to the Web version of this article.)

Zwaan et al. (2018a). However, as already remarked by the latter authors, the tendency of the rifts to grow toward each other suggests that a 2 H distance between rifts is not enough to prevent them interacting under orthogonal extension conditions. This somewhat contradicts the findings by Zwaan et al. (2016), but is in accordance with similar models with high underlaps (small angle φ) by Zwaan and Schreurs (2017). Other analogue and numerical modellers have also reported the development of rift pass structures and the associated rotation of the central block due to extension gradients along both rift segments (e.g. Hieronymus, 2004; Acocella, 2008; Tentler and Acocella, 2010, Allken et al., 2011, 2012, Molnar et al., 2017, 2018; Zwaan et al., 2018a; Glerum et al., 2020, Fig. 7d, g).

The transfer zone structures developing in our φ ≈ 45° and 30° experiments (Figs. 3, 4 and 7b) are a consequence of both the seed geometry and the rift propagation direction. Similar behaviour is found in models described by Acocella et al. (1999), Hieronymus (2004), Tentler and Acocella (2010) and Allken et al. (2011, 2012) (Fig. 7e, h). Transfer zone development is known to be promoted by oblique extension and smaller rift offset (Hus et al., 2005; Allken et al., 2011; Zwaan et al., 2016, Zwaan et al., 2018a; Zwaan and Schreurs, 2017). We see that both propagating rift branches almost directly grow into each other, forming a continuous transfer zone basin bounded by through-going boundary faults. However, the occurrence of minor sub-basins or similar structures in several of the φ = 30° experiments that remain separated at depth (Figs. 4c, 6 and A1c-f) indicates the transition to the next rift linkage mode involving accommodation zones.

Our experiments with φ ≤ 20° typically develop such accommodation zones, which are characterized by the presence of large right-stepping sub-basins between the main right-stepping rift segments (Figs. 3, 4 and 7c). Such features are also observed in the models by Tentler and Accocella (2010) and Allken et al. (2011, 2012). The occurrence of these sub-basins is probably related to the two main rift segments focussing deformation, leading to subsequent localization of faulting in the centre of the underlap zone. As shown in Zwaan et al. (2020a) and model R17 (Fig. 3), faulting in this type of experiment will normally strongly deflect to the sidewalls when not sufficiently

concentrated along seeds along the model axis. But when both main rift segments are well-developed, deformation is probably directed to the central axis of the model, although still some 50% of extension is taken up by sidewall boundary effects in this type of experiments (Zwaan et al., 2020a). Since the regional extension field is (near-)orthogonal to the seeds (Fig. 2d'), these en echelon basins subsequently develop approximately along-strike, as illustrated in model O11 (Fig. 7c).

We thus find that the sequence of rift interaction structures as a function of angle φ in our experiments are also present in previous analogue and numerical modelling studies. Yet it is important to stress that although the resulting structures are similar, the initial parameters may be somewhat different (e.g. compare the offset and underlap angle φ between models O1, O7 and O11 with those in the numerical models by Allken et al., 2011, Fig. 7a–f). Modelling efforts indeed reveal that factors as strain weakening, changing brittle-viscous coupling and difference in cohesion of brittle materials may easily cause a shift to another rift interaction style (Allken et al., 2011, 2012). This sensitivity to minor differences is perhaps best illustrated by the structural variability in our $\varphi \approx 30^{\circ}$ models (Fig. A1). Furthermore, the boundary conditions of these previously published models vary widely (e.g. brittle-only or brittle-viscous layering, base plate or rubber base, fast or slow extension etc.), which are all known to have important effects on structural style (Zwaan et al., 2019).

Such differences may for example cause the lack of strike-slip transfer faults (i.e. strike-slip faults oriented [sub-]parallel to the extension direction that are potential precursors of oceanic transform faults) in our experiments. This discrepancy could be due to for instance the lack of strain weakening in our models (e.g. Hieronymus, 2004; Allken et al., 2011), too low rift offset or too high viscosity in the lower crust analogue (Allken et al., 2012). Alternatively, cohesion in our brittle material may be too low, since models presented in O'Bryan et al. (1975) and Tentler and Acocella (2010) develop clear transfer/transform faults in materials with a relatively high cohesion, which probably promotes rigid block motion. Analogue models with plate base set-ups force transfer zone formation along the basal velocity discontinuity (VD, i.e. the edge of the base plate) (Mauduit and Dauteuil, 1996; Acocella et al., 1999; Dauteuil et al., 2002). Yet other models involving a different set-up show that rift-perpendicular structural weaknesses can also remain inactive (Zwaan and Schreurs, 2017; Molnar et al., 2019). Acocella et al. (2008) furthermore suggest that additional rift-parallel extension may help to establish strike-slip transfer/transform faults instead of an overlapping spreading centre configuration. Finally, the relatively limited total stretching in our models could play an important role as well, since previous work suggests that the initial transfer zones we find in our models may develop into (oceanic) transform faults after larger degrees of extension (e.g. Oldenburg and Brune, 1972, 1975; Acocella et al., 2005; Gerya, 2013; Ammann et al., 2018). Some modelling work even suggests that an established transform fault can destabilize and return to an overlapping spreading zone structure (e.g. Gerya, 2013; Oldenburg and Brune, 1975).

4.3. Comparison with natural examples

4.3.1. Rift interaction zones

Clear examples of rift pass structures are found in East Africa in the form of the Western and Eastern branches of the EARS, with the Victoria plate in between (Fig. 1b), as well as the Danakil Block in Afar (Figs. 1a and 8a). In both cases, the block between both rift segments is clearly pivoting about a vertical rotation axis (e.g. McClusky et al., 2010; Saria et al., 2014; Glerum et al., 2020). Oceanic examples (i.e. overlapping spreading centers) occur along the mid-oceanic ridges in the Pacific and North Atlantic (Tentler and Acocella, 2010, and references therein, Fig. 8b).

It is important to note that the initiation of a rift pass in continental settings may, if extension continues, lead to the formation of microcontinents such as Jan Mayen in the NE Atlantic (Müller et al., 2001; Peron-Pinvidic et al., 2012a, b, Fig. 8b). Here, initial (Early Eocene) break-up took place along the Ægir Ridge (Talwani and Eldholm, 1977). However, migration of the Iceland hotspot caused the formation of the Kolbeinsey rift in Late Oligocene times (Nunns, 1982), which subsequently became the dominant spreading center, shutting down tectonic activity along the Ægir Ridge. As a consequence, the Jan Mayen block

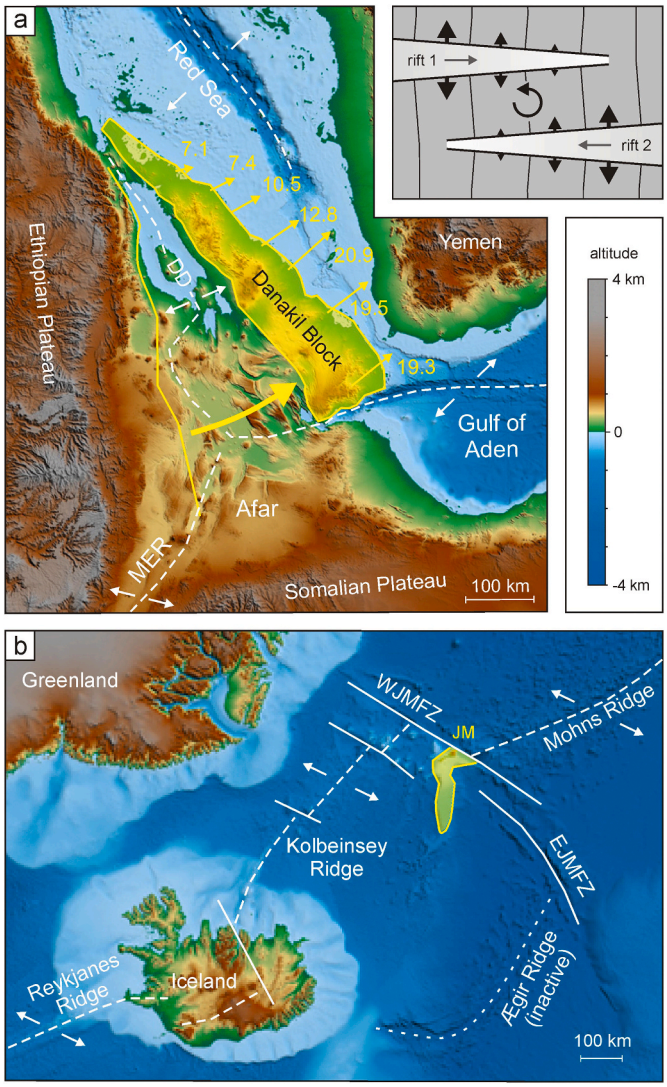

Fig. 8. Rotation of a continental sliver and creation of a microcontinent due to two overlapping rift segments (see inset sketch, modified after Zwaan et al., 2018a). (a) Danakil block (yellow) in the Afar triple junction, which rotates away from Africa (yellow arrow and GPS vectors in mm/yr) due to the combined action of the Red Sea rift axis to the east and the Danakil/Afar rift axis to the west. Note how the triangular shape of the Afar Depression and the southward increasing extension is mirrored in the Red Sea. DD: Danakil Depression, MER: Main Ethiopian Rift. For location see Fig. 1a. Image modified after ArRahjehi et al. (2010), McClusky et al. (2010), Saria et al. (2014), and La Rosa et al. (2019). (b) Jan Mayen microcontinent (yellow) in the North Atlantic, formed due to a rift jump from the now inactive Aegir Ridge to the Kolbeinsey Ridge that cut off a continental sliver (indicated by yellow dotted outline) from Greenland. The arrow indicates rift propagation direction. EJMFZ = East Jan Mayen Fracture Zone, JM = Jan Mayen, RR = Reykjanes Ridge, WJMFZ = West Jan Mayen Fracture Zone. Modified after Acocella et al. (1999), Dick et al. (2003), Gaina et al. (2009), Peron-Pinvidic et al. (2012a, b) and Blischke et al. (2016). Background topography and bathymetry is derived from GEBCO (2020) and the IBCAO maps (Jakobsson et al., 2012). (For interpretation of the references to colour in this figure legend, the reader is referred to the Web version of this article.)

now forms a block of continental material surrounded by oceanic lithosphere (Peron-Pinvidic et al., 2012a, b; Blischke et al., 2016 and references therein).

A currently developing microcontinent is the Danakil Block in the Afar region of Africa (Fig. 8a), which is splitting away from Africa due to the interaction of rifting in the Afar Depression/Danakil Depression to its west and the Red Sea to its east (e.g. Mohr, 1970). The associated anticlockwise rotation occurs as a result of the overlapping extension gradients in both rifts (e.g. Oldenburg and Brune, 1975; Bubeck et al., 2017; Zwaan et al., 2018a, Glerum et al., 2020, Figs. 7a and 8). Interestingly and similarly to the Jan Mayen example, the influence of the Afar plume is expected to enable complete future continent break-up on both sides of the block, as the influence of a mantle anomaly may be a necessity to fully develop a true microcontinent (Dubinin et al., 2018; Molnar et al., 2017, 2018).

Transfer zones with continuous (boundary) fault structures can be found at the Rhine-Bresse (or Burgundy) Transfer Zone (e.g. Dèzes et al., 2004; Ustaszewski et al., 2005), the Rio Grande Basin in the USA (Aldrich, 1986), as well as various subbasins along the EARS, such as the Pakwach Basin between the Rhino-Camp and Albert Rift basins (e.g. Corti, 2012; Abeinomugisha and Njabire, 2012, Fig. 1b, b'). A feature that we, however, do not observe in our models is the development of transform faults such as the East- and West Jan Mayen Fracture Zones (Fig. 8) and on a larger scale, the Knipovic Ridge (Fig. 1c). An explanation of this lack of transform fault development may be (amongst others, see section 4.2) the small amount of extension in our models. The initial transfer zones we find in our models may develop into (oceanic) transform fault systems after larger degrees of extension (Acocella et al., 2005; Gerya, 2013; Amman et al., 2018). As a matter of fact, the Knipovich Ridge does still have a rather oblique orientation with respect to the rift axes in the North Atlantic and Arctic Ocean so that it could nicely fit such a scenario (Fig. 1c).

Our models with substantial underlap ($\varphi \leq 20°$) are characterized by the presence of a sub-basin between both rift segments (Figs. 3 and 7c). Such structures are however challenging to distinguish in nature due to their resemblance to en echelon rift basins formed during oblique extension, e.g. in the North Sea Rift System, (Erratt et al., 1999, 2010). Similar basins, as well as varying extension rates and directions also exist along the branches of the EARS (Fig. 1b, b'). Yet we believe that the Rwenzori Rift, which represents the transition between the Albert and Kivu Rifts within an area undergoing near-orthogonal extension, may represent a proper sub-basin accommodation zone as observed in our models (Corti, 2012; Saria et al., 2014, Fig. 1b'). Other examples may be found in the Utah Canyonlands and the North Sea Viking Graben (Trudgill and Cartwright, 1994; Fossen et al., 2010; Allken et al., 2011).

4.3.2. *Effects of extension gradients on developing rift systems: the EARS*

The modelling studies by Molnar et al. (2017, 2018, 2019) Mondy et al. (2018) and Zwaan et al. (2020) all show extension velocity gradients associated with rotational extension causing rift propagation and the development of V-shaped basins. Clear oceanic examples can be found in the Red Sea, Gulf of Aden and the Arctic Gakkel Ridge (Fig. 1). Yet for an assessment of the effects of extension gradients on rift interaction structures in a young continental rift, we turn to the Western Rift in Africa (i.e. the western branch of the EARS, Fig. 1b, b'). The Western Rift with its various sub-basins curving around the western boundary of the Victoria plate is currently subject to a positive extension velocity gradient from the Rhino-Camp Basin in the north (1.3 mm/yr) to the Rukwa Rift in the south (2.9 mm/yr, Saria et al., 2014, Fig. 1b'). These data suggest that the Western Rift should have propagated from south to north, with the youngest segments in the northern tip. Yet the opposite seems to be true: although establishing the timing of rifting is challenging, rifting is thought to have started around 17 Ma in the Albert Rift area and most likely propagated southward (Ebinger, 1989; Kampunzu et al., 2015; Macgregor, 2015), posing an apparent paradox.

The solution lies in the combined large-scale motion of the Somalian, Victoria and Rovuma plates with respect to the Nubian plate (Fig. 1a and b). Together these plates follow a clockwise (westward) rotation and a north-south extension gradient that is very clear when summing up the vectors at every latitude (Fig. 1b). We propose a scenario (Fig. 9), in which this rotation about a more or less stable Euler pole, situated near the tip of South Africa) (Saria et al., 2014; DeMets and Merkouriev, 2016, Fig. 1b) leads to the general southward propagation of rifting along the EARS that is described by Chorowicz (2005) (and references therein). During the first stage (ca. 20–25 Ma), rifting occurred mostly along the Kenya Rift (Fig. 9a and Bonini et al., 2005). As extension continued, rifting jumped into the Albert Rift area around 17 Ma (Macgregor, 2015), and moved southward from there (Fig. 9b, Ebinger et al., 1989; Kampunzu et al., 2015). Here the Western Rift becomes dominant over the Kenya rift, causing the counterclockwise rotation of the Victoria plate in a rift pass setting (Glerum er al. 2020). Towards the south, the Malawi rift may have developed as late as 9 or even 5 Ma (Ebinger et al., 1993; McCartney and Scholz, 2016), a timing which, although debated (Schillington et al., 2020 and references therein), would fit very well with this large-scale scenario of a southward propagating rift system due to the large-scale rotation of the Somalian plate (Fig. 9c).

The proposed scenario for the EARS is itself supported by our

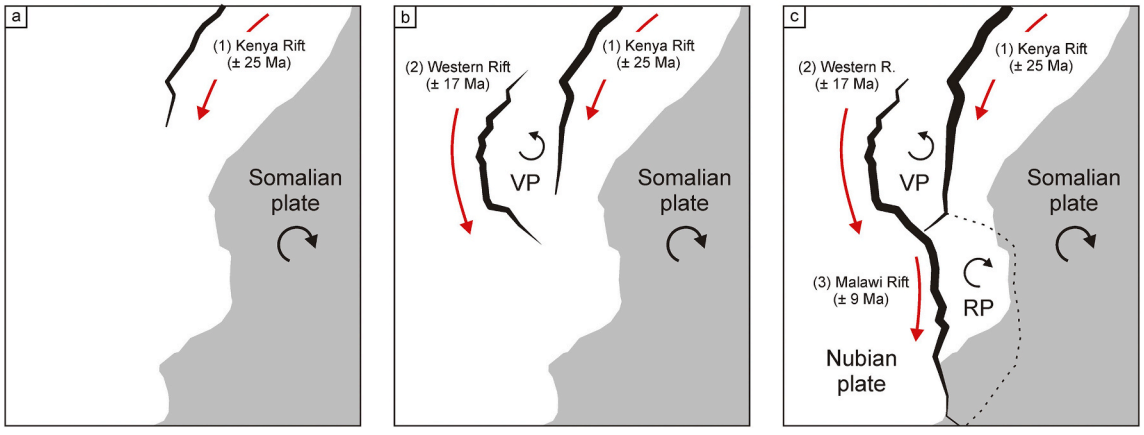

Fig. 9. Proposed evolution of the East African Rift System (EARS) as a result of rotational extension and southward rift propagation. (a) Rift initiation along the Kenya Rift around 20–25 Ma (Bonini et al., 2005). (b) Westward rift jump into the Albert Rift area around 17 Ma and dominant southward rift propagation along the Western Rift, leading to rotation of the Victoria plate (VP) due to the rift pass configuration. (c) Opening of the Malawi rift around 9 Ma and further southward (Ebinger et al., 1993; McCartney and Scholz, 2016). The development of the Rovuma plate (RP) is not clearly defined as deformation is minor with respect to the other rift axes (Fig. 1b). The width of the rift segments represents the extension gradients along the EARS. Modified after Saria et al. (2014).

rotational extension rift pass models, in which the rift basin farthest away from the rotation axis forms first, followed by the rift segment closer to the rotation axis and rift propagation away from the rift pass zone (Figs. 3b and 5a). By contrast, such delayed rift arm development and propagation away from the rift pass does not occur in orthogonal extension experiments (Fig. 4a). These insights may be highly useful when interpreting the evolution of other large-scale rift systems with important rift interaction structures, such as the Knipovitch ridge in the North Atlantic/Artic (Fig. 1c), and the general break-up between South America and Africa in the South Atlantic (e.g. Heine et al., 2013).

5. Conclusion

In this paper we apply analogue tectonic models to assess the differences between rift interaction structures developing in either orthogonal extension or rotational extension settings. Our model results lead us to the following conclusions:

- Although rotational extension and orthogonal extension produce quite different large-scale structures, local features in a rotational extension systems can be regarded as forming in an orthogonal extension setting.
- However, the extension gradient in rotational extension models will cause more deformation farther away from the rotation axis, leading to important differences in maturity between both rift segments, and a delay in rift interaction zone development with respect to the orthogonal extension equivalent. We also find that rift segments may propagate in two directions rather than one due to rotational extension.
- Various degrees of initial rift underlap produce three basic modes of rift linkage structures. Low underlap (high angle φ of $>$ ca. 40°) experiments develop rift pass structures where rift branches grow past and around each other. With increasing underlap (φ = ca. 40°), transfer zone basins with faults directly connecting both rift segments develop, although CT imagery shows that such transfer zone structures may remain separate at depth. High degrees of underlap ($\varphi \leq 30°$) tend to result in accommodation zones with en echelon sub-basins. Several of these structures are found in previous model studies and in nature.
- Our models do not develop the (precursor) transform faults observed in previous analogue and numerical modelling studies, which is likely due to differences in experimental boundary conditions.
- We explain the structures and timing of the East African Rift System by means of a southward rift propagation scenario involving a rift pass around the Victoria plate that could only have occurred by means of rotational extension. Such applications of rotational extension models may also be useful for the interpretation of other large-scale rift systems.

Data availability

Animations and overview images of the models presented in this study are compiled in a GFZ Data Services open access data publication (Zwaan and Schreurs, 2020), available online at: https://doi.org/10.5880/fidgeo.2020.031.

CRediT authorship contribution statement

Frank Zwaan: Conceptualization, Methodology, Investigation, Writing - original draft, Visualization, Data curation. **Guido Schreurs:** Writing - review & editing, Supervision, Project administration, Funding acquisition, Resources.

Declaration of competing interest

The authors declare that they have no known competing financial interests or personal relationships that could have appeared to influence the work reported in this paper.

Acknowledgements

We would like to thank Nicole Schwendener for helping us with the CT-scanning, the University of Bern (via Marco Herwegh) for funding both the upgrading of the orthogonal extension apparatus and the development of the new rotational extension machine. We also acknowledge the engineers from IPEK Rapperswil (Theodor Wüst, Reto Gwerder, Rudolf Kamber, Michael Ziltener, Christoph Zolliker and Claude Grau), who realized the improvements to the existing orthogonal extension machine and subsequently designed and constructed the new rotational extension machine. Moreover, we are grateful to the Berne University Science Foundation, which provided generous financial support for the new rotational extension machine, as well and the Swiss National Science Foundation, the principal funder of this project (grant no. 200021_147046, http://p3.snf.ch/project-147046). Reviewers Sascha Brune and Tim Dooley are kindly acknowledged for their detailed and constructive feedback, and we thank Kirsten Elger for helping us creating the GFZ data publication containing our supplementary material (Zwaan and Schreurs, 2020).

Appendix A. Rift linkage zone variability in orthogonal extension models

Although Fig. 3 displays the models that provide a best fit, i.e. a logical order of structures, we observe that the models exhibit a certain structural variability; some models have been repeated, occasionally yielding results that seem more typical of models with a slightly lower or higher underlap angle. For example, the $\varphi = 30°$ orthogonal extension setting can either produce a continuous transfer zone basin (Model O8, Fig. A1a, b), an accommodation zone with an en echelon basin between both main rifts (Model O10, Fig. A1e, f) or an intermediate form (Model O9 in Figs. 3a, 4c, 6, A1c, d). In fact, the surface structure of Model O9 seems closer to the continuous transfer zone basin observed in Model O8 (Figs. 3a, 4c, 6 and A1a, c) , yet when the sand is removed to reveal the topography of the deformed viscous layer (Fig. A1b, d, f), the deeper structure shows more affinity with that of Model O10 than the clean continuous trace of the Model O8 transfer zone. Furthermore, the transfer zone from Model O8 is quite similar to the one in Model O7 ($\varphi = 40°$, Figs. 3a, 4b, 7b and A1a, c), as is the accommodation zone from Model O10 to the one in Model O11 ($\varphi = 20°$, Fig. 3a, 4d, 7c and A1e).

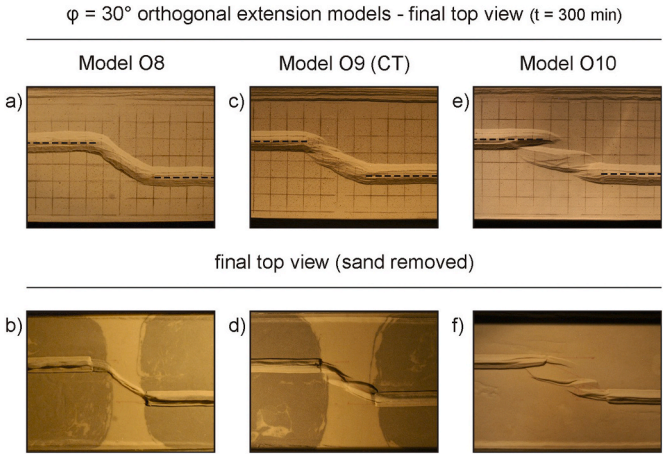

Fig. A1. Structural variation between Models O8-10 (orthogonal extension, φ = 30°) after 300 min (e = 4 cm). The colour differences in the top views without sand cover (b, d, f) are due to differently coloured corundum sand used for the viscous mixture and have no influence on the material's rheology.

Appendix B. Rift localization in rotational extension models

Also the φ = 30° rotational extension models have a significant variety in their rift linkage structures (Fig. B1). Model R8 (Figs. 3b and B1b) is quite similar to its orthogonal equivalent model O9 (Figs. 3a, 4d and 6). Yet various models (e.g. Models R9 and R17, Figs. 3b and B1a) form a dominant rift basin on the left-hand seed, and a right-hand, delayed and underdeveloped rift basin. This late development of faulting along the seed nearest to the rotation axis is shown to obstruct rift linkage (Figs. 3b and B1a) and is probably linked to the low amount of extension there, compared to the areas farther away from the rotation axis. When the rift segment near the rotation axis fails to develop early on, the boundary effects along the sidewalls (possibly propagating from the area farther away from the rotation axis) must account for most if not all deformation in that sector (similar to observations by Zwaan et al., 2020a). In Model R8 (Figs. 3b and B1b) by contrast, the secondary rift arm is considerably more developed, and a transfer zone is established. A test with a thicker seed (1.5 mm diameter compared to the standard 1 mm) on the right-hand seed (Model R13, Fig. B1c) was performed to assess this effect: the model establishes early localization and proper rift linkage via a transfer zone structure. In nature, such (propagating) boundary effects should not occur and we can safely state that the models with more localized deformation and subsequent rift linkage zone development best represent natural settings.

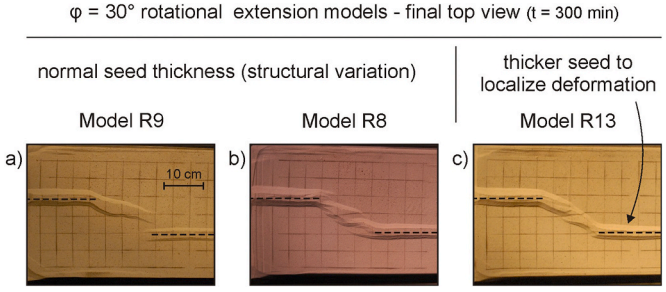

Fig. B1. Structural variations between Models R8, R9 and R13 (rotational extension, φ = 30°) after 300 min (e = 4 cm). These are zoom-ins on the rift interaction area, the rotation axis is situated to the right, outside of the depicted model domain.

References

Abeinomugisha, D., Njabire, N., 2012. Transfer Zones and Hydrocarbon Accumulation in the Albertine Graben of the East African Rift System. Search and Discovery Article #10401. http://www.searchanddiscovery.com/documents/2012/10401abeinomugisha/ndx_abeinomugisha.pdf.

Acocella, V., Faccenna, C., Funiciello, R., Rossetti, F., 1999. Sand-box modelling of basement-controlled transfer zones in extensional domains. Terra Nova 11, 149–156. https://doi.org/10.1046/j.1365-3121.1999.00238.x.

Acocella, V., Morvillo, P., Funiciello, R., 2005. What controls relay ramps and transfer faults within rift zones? Insights from analogue models. J. Struct. Geol. 27, 397–408. https://doi.org/10.1016/j.jsg.2004.11.006.

Acocella, V., 2008. Transform faults or Overlapping Spreading Centers? Oceanic ridge interactions revealed by analogue models. Earth Planet Sci. Lett. 265, 379–385. https://doi.org/10.1016/j.epsl.2007.10.025.

Aldrich, M.J., 1986. Tectonics of the Jemez Lineament in the Jemez Mountains and Rio Grande Rift. J. Geophys. Res. 91, 1753–1762. https://doi.org/10.1029/JB091iB02p01753.

Allken, V., Huismans, R.S., Thieulot, C., 2011. Three-dimensional numerical modeling of upper crustal extensional systems. J. Geophys. Res. 116, B10409 https://doi.org/10.1029/2011JB008319.

Allken, V., Huismans, R.S., Thieulot, C., 2012. Factors controlling the mode of rift interaction in brittle-ductile coupled systems: A 3D numerical study. Geochem. Geophys. Geosys. 13, Q05010. https://doi.org/10.1029/2012GC004077.

Amman, N., Liao, J., Gerya, T., Ball, P., 2018. Oblique continental rifting and long transform fault formation based on 3D thermomechanical numerical modeling. Tectonophysics 746, 106–120. https://doi.org/10.1016/j.tecto.2017.08.015.

ArRajehi, A., McClusky, S., Reilinger, R., Daoud, M., Alchalbi, A., Ergintav, S., Gomez, F., Sholan, J., Bou-Rabee, F., Ogubazghi, G., Haileab, B., Fisseha, S., Asfaw, L., Mahmoud, S., Rayan, A., Bendik, R., Kogan, L., 2010. Geodetic constraints on present-day motion of the Arabian Plate: Implications for Red Sea and Gulf of Aden rifting. Tectonics 29,. https://doi.org/10.1029/2009TC002482. TC3011.

Bellahsen, N., Faccenna, C., Funiciello, F., Daniel, J.M., Jolivet, L., 2003. Why did Arabia separate from Africa? Insights from 3-D laboratory experiments. Earth Planet Sci. Lett. 216, 365–381. https://doi.org/10.1016/S0012-821X(03)00516-8.

Benes, V., Scott, S.D., 1996. Oblique rifting in the Havre Trough and its propagation into the continental margin of New Zealand: Comparison with analogue experiments. Mar. Geophys. Res. 18, 189–201. https://doi.org/10.1007/BF00286077.

Blischke, A., Gaina, C., Hopper, J.R., Péron-Pinvidic, G., Brandsdóttir, B., Guarnieri, P., Erlendsson, Ö., Gunnarsson, K., 2016. The Jan Mayen microcontinent: an update of its architecture, structural development and role during the transition from the Ægir Ridge to the mid-oceanic Kolbeinsey Ridge. In: Péron-Pinvidic, G., Hopper, J.R., Stoker, M.S., Gaina, C., Doornenbal, J.C., Funck, T., Árting, U.E. (Eds.), The NE Atlantic Region: A Reappraisal of Crustal Structure, Tectonostratigraphy and Magmatic Evolution. Geological Society, London, Special Publications 447, pp. 299–337. https://doi.org/10.1144/SP447.5.

Bonini, M., Corti, G., Innocenti, F., Manetti, P., Mazzarini, F., Abebe, T., Pecskay, Z., 2005. Evolution of the Main Ethiopian Rift in the frame of Afar and Kenya rifts propagation. Tectonics 24,, TC1007. https://doi.org/10.1029/2004TC001680.

Bosworth, W., Huchon, P., McClay, K., 2005. The Red Sea and Gulf of Aden basins. J. Afr. Earth Sci. 43, 334–378. https://doi.org/10.1016/j.jafrearsci.2005.07.020.

Brune, S., Popov, A.A., Sobolev, S.V., 2012. Modeling suggests that oblique extension facilitates rifting and continental break-up. J. Geophys. Res. 117, B08492. https://doi.org/10.1029/2011JB008860.

Brune, S., 2018. Forces within continental and oceanic rifts: numerical modeling elucidates the impact of asthenospheric flow on surface stress. Geology 46, 191–192. https://doi.org/10.1130/focus022018.1.

Bubeck, A., Wlaker, R.J., Imber, J., Holdsworth, R.E., MacLeod, C.J., Holwell, D.A., 2017. Extension parallel to the rift zone during segmented fault growth: application to the evolution of the NE Atlantic. Solid Earth 8, 1161–1180. https://doi.org/10.5194/se-8-1161-2017.

Buck, W.R., 1991. Models of continental lithospheric extension. J. Geophys. Res. 96, 20,161–20,178. https://doi.org/10.1029/91JB01485.

Carlo AG, 2020. Carlo Bernasconi AG, Switzerland. Company website: https://carloag.ch.

Childs, C., Watterson, J., Walsh, J.J., 1995. Fault overlap zones within developing normal fault systems. J. Geol. Soc. 152, 535–549. https://doi.org/10.1144/gsjgs.152.3.0535.

Chorowicz, J., 2005. The East African rift system. J. Afr. Earth Sci. 43, 379–410. https://doi.org/10.1016/j.jafrearsci.2005.07.019.

Corti, G., 2012. Evolution and characteristics of continental rifting: Analog modeling-inspired view and comparison with examples from the East African Rift System. Tectonophysics 522–523, 1–33. https://doi.org/10.1016/j.tecto.2011.06.010.

Corti, G., Bonini, M., Sokoutis, D., Innocenti, F., Manetti, P., Cloetingh, S., Mulugeta, G., 2004. Continental rift architecture and patterns of magma migration: A dynamic analysis based on centrifuge models. Tectonics 23,, TC2012. https://doi.org/10.1029/2003TC001561.

Corti, G., Van Wijk, J., Cloetingh, S., Morley, C.K., 2007. Tectonic inheritance and continental rift architecture: Numerical and analogue models of the East African Rift system. Tectonics 26,, TC6006. https://doi.org/10.1029/2006TC002086.

Dauteuil, O., Bourgeois, O., Mauduit, T., 2002. Lithosphere strength controls oceanic transform zone structure: insights from analogue models. Geophys. J. Int. 150, 706–714. https://doi.org/10.1046/j.1365-246X.2002.01736.x.

DeMets, C., Merkouriev, S., 2016. High-resolution estimates of Nubia–Somalia plate motion since 20 Ma from reconstructions of the Southwest Indian Ridge, Red Sea and Gulf of Aden. Geophys. J. Int. 207, 317–332. https://doi.org/10.1093/gji/ggw276.

Deprez, A., Doubre, C., Masson, F., Ulrich, P., 2013. Seismic and aseismic deformation along the East African Rift System from a reanalysis of the GPS velocity field of Africa. Geophys. J. Int. 193, 1353–1369. https://doi.org/10.1093/gji/ggt085.

Dèzes, P., Schmid, S.M., Ziegler, P.A., 2004. Evolution of the European Cenozoic Rift System: interaction of the Alpine and Pyrenean orogens with their foreland lithosphere. Tectonophysics 389, 1–33. https://doi.org/10.1016/j.tecto.2004.06.011.

Dick, H.J.B., Lin, J., Schouten, H., 2003. An ultra-slow spreading class of oceanic ridge. Nature 426, 405–412. https://doi.org/10.1038/nature02128.

Dubinin, E.P., Grokholsky, A.L., Makushiba, A.I., 2018. Physical modeling of the formation conditions of microcontinents and continental marginal plateaus. Izvestiya Phys. Solid Earth 54, 66–78. https://doi.org/10.1134/S1069351318010056.

Dyksterhuis, S., Rey, P., Müller, R.D., Moresi, L., 2007. Effects of initial weakness on rift architecture. In: Karner, G.D., Manatschal, G., Pinheiro, L.M. (Eds.), Imaging, Mapping and Modelling Continental Lithosphere Extension and Breakup. Geological Society, London, Special Publications 282, pp. 443–455. https://doi.org/10.1144/SP282.18.

Ebinger, C.J., 1989. Tectonic development of the western branch of the East African rift system. GSA Bulletin 101, 885–903. https://doi.org/10.1130/0016-7606(1989)101<0885:TDOTWB>2.3.CO;2.

Ebinger, C.J., Deino, A.L., Tesha, A.L., Becker, T., Ring, U., 1993. Tectonic controls on rift basin morphology: Evolution of the northern Malawi (Nyasa) Rift. J. Geophys. Res. 98 https://doi.org/10.1029/93JB01392, 17,821-17,836.

Elmohandes, S.-E., 1981. The central European graben system: rifting imitated by clay modelling. Tectonophysics 73, 69–78. https://doi.org/10.1016/0040-1951(81)90174-8.

Erratt, D., Thomas, G.M., Wall, G.R.T., 1999. The evolution of the Central North Sea Rift. In: Fleet, A.J., Boldy, S.A.R. (Eds.), Geological Society, London, Petroleum Geology Conference Series, vol. 5, pp. 63–82. https://doi.org/10.1144/0050063.

Erratt, D., Thomas, M., Hartley, N.R., Musum, R., Nicholson, P.H., Spisto, Y., 2010. North Sea hydrocarbon systems: some aspects of our evolving insights into a classic hydrocarbon province. In: Vining, B.A., Pickering, S.C. (Eds.), Petroleum Geology: From Mature Basins to New Frontiers – Proceedings of the 7th Petroleum Geology Conference. Geological Society, London, Petroleum Geology Conference Series, 7, pp. 37–56.

Faulds, J.E., Varga, R.J., 1998. The role of accommodation zones and transfer zones in the regional segmentation of extended terranes. In: Faulds, J.E., Stewart, J.H. (Eds.), Accommodation Zones and Transfer Zones: the Regional Segmentation of the Basin and Range Province. GSA Special Paper, 323, pp. 1–46. https://doi.org/10.1130/0-8137-2323-X.1.

Fossen, H., Schultz, R.A., Rundhovde, E., Rotevatn, A., Buckley, S.J., 2010. Fault linkage and graben stepovers in the Canyonlands (Utah) and the North Sea Viking Graben, with implications for hydrocarbon migration and accumulation. AAPG Bull. 94 (5), 597–613. https://doi.org/10.1306/10130909088.

Gaina, C., Gernigon, L., Ball, P., 2009. Palaeocene–Recent plate boundaries in the NE Atlantic and the formation of the Jan Mayen microcontinent. J. Geol. Soc. London 166, 601–616. https://doi.org/10.1144/0016-76492008-112.

GEBCO, 2020. Global Bathymetric map of the Ocean. https://www.gebco.net.

Gerya, T.V., 2013. Three-dimensional thermomechanical modeling of oceanic spreading initiation and evolution. Phys. Earth Planet. In. 214, 35–52. https://doi.org/10.1016/j.pepi.2012.10.007.

Glerum, A., Brune, S., Stamps, D.S., Strecker, M.R., 2020. Victoria continental microplate dynamics controlled by the lithospheric strength distribution of the East African Rift. Nat. Commun. 11, 2881 https://doi.org/10.1038/s41467-020-16176-x.

Handin, J., 1969. On the Coulomb–Mohr failure criterion. J. Geophys. Res. 74, 5343–5348. https://doi.org/10.1029/JB074i022p05343.

Heine, C., Zoethout, J., Müller, R.D., 2013. Kinematics of the South Atlantic rift. Solid Earth 4, 215–253. https://doi.org/10.5194/se-4-215-2013.

Heron, P.J., Peace, A.L., McCaffrey, K.J.W., Welford, J.K., Wilson, R., van Hunen, J., Pysklywec, R.N., 2019. Segmentation of Rifts Through Structural Inheritance: Creation of the Davis Strait. Tectonics 38, 2411–2430. https://doi.org/10.1029/2019TC005578.

Hieronymus, C.H., 2004. Control on seafloor spreading geometries by stress- and strain-induced lithospheric weakening. Earth Planet Sci. Lett. 222 (1), 177–189. https://doi.org/10.1016/j.epsl.2004.02.022.

Hubbert, M.K., 1937. Theory of scaled models as applied to the study of geological structures. GSA Bulletin 48, 1459–1520. https://doi.org/10.1130/GSAB-48-1459.

Hus, R., Acocella, V., Funicello, R., De Batist, M., 2005. Sandbox models of relay ramp structure and evolution. J. Struct. Geol. 27, 459–473. https://doi.org/10.1016/j.jsg.2004.09.004.

Jaeger, J.C., Cook, N.G.W., 1976. Fundamentals of Rock Mechanics. Chapman & Hall, Wiley, New York.

Jakobsson, M., Mayer, L., Coakley, B., Dowdeswell, J.A., Forbes, S., Fridman, B., Hodnesdal, H., Noormets, R., Pedersen, R., Rebesco, M., Schenke, H.-W., Zarayskaya, Y., Accettella, D., Armstrong, A., Anderson, R.M., Bienhoff, P., Camerlenghi, A., Church, I., Edwards, M., Gardner, J.V., Hall, J.K., Hell, B., Hestvik, O.B., Kristoffersen, Y., Marcussen, C., Mohammad, R., Mosher, D., Nghiem, S.V., Pedrosa, M.T., Travaglini, P.G., Weatherall, P., 2012. The International Bathymetric Chart of the Arctic Ocean (IBCAO) Version 3.0. Geophys. Res. Lett. 39, L12609 https://doi.org/10.1029/2012GL052219.

Kampunzu, A.B., Bonhomme, M.G., Kanika, M., 2015. Geochronology of volcanic rocks and evolution of the Cenozoic Western Branch of the East African Rift System. J. Afr. Earth Sci. 26, 441–461. https://doi.org/10.1016/S0899-5362(98)00025-6.

Koopmann, H., Brune, S., Franke, D., Breuer, S., 2014. Linking rift propagation barriers to excess magmatism at volcanic rifted margins. Geology 42, 1071–1074. https://doi.org/10.1130/G36085.1.

Kydonakis, K., Brun, J.-P., Sokoutis, D., 2015. North Aegean core complexes, the gravity spreading of a thrust wedge. J. Geophys. Res.: Solid Earth 120. https://doi.org/10.1002/2014JB011601.

La Rosa, A., Pagli, C., Keir, D., Sani, F., Corti, G., Wang, H., Possee, D., 2019. Observing Oblique Slip During Rift Linkage in Northern Afar. Geophys. Res. Lett. 46, 10782–10790. https://doi.org/10.1029/2019GL084801.

Larsen, P.-H., 1988. Relay structures in a Lower Permian basement-involved extension system, East Greenland. J. Struct. Geol. 10, 3–8. https://doi.org/10.1016/0191-8141(88)90122-8.

Le Calvez, J.H., Vendeville, B.C., 2002. Experimental designs to model along-strike fault interaction. In: Schellart, W.P., Passchier, C. (Eds.), Analogue Modelling of Large-Scale Tectonic Processes. J. Virtual Explor, 7, pp. 1–17. https://doi.org/10.3809/jvirtex.2002.00043.

Le Pourhiet, L., Chamot-Rooke, N., Delescluse, M., May, D.A., Watremez, L., Pubellier, M., 2018. Continental break-up of the South China Sea stalled by far-field compression. Nat. Geosci. 11, 605–609. https://doi.org/10.1038/s41561-018-0178-5.

Macgregor, D., 2015. History of the development of the East African Rift System: A series of interpreted maps through time. J. Afr. Earth Sci. 101, 232–252. https://doi.org/10.1016/j.jafrearsci.2014.09.016.

Martin, A.K., 1984. Propagating rifts: Crustal extension during continental rifting. Tectonics 3, 611–617. https://doi.org/10.1029/tc003i006p00611.

Mauduit, T., Dauteuil, O., 1996. Small-scale models of oceanic transform zones. J. Geophys. Res. 101, 20,195–20,209. https://doi.org/10.1029/96JB01509.

McCartney, T., Scholz, C.A., 2016. A 1.3 million year record of synchronous faulting in the hangingwall and border fault of a half-graben in the Malawi (Nyasa) Rift. J. Struct. Geol. 91, 114–129. https://doi.org/10.1016/j.jsg.2016.08.012.

McClay, K.R., White, M.J., 1995. Analogue modelling of orthogonal and oblique rifting. Mar. Petrol. Geol. 12, 137–151. https://doi.org/10.1016/0264-8172(95)92835-K.

McClusky, S., Reilinger, R., Ogubazghi, G., Amleson, A., Healeb, B., Vernant, P., Sholan, J., Fisseha, S., Asfaw, L., Bendick, R., Kogan, L., 2010. Kinematics of the southern Red Sea–Afar triple junction and implications for plate dynamics. Geophys. Res. Lett. 37, L05301 https://doi.org/10.1029/2009GL041127.

Michon, L., Merle, O., 2000. Crustal structures of the Rhinegraben and the Massif Central grabens: An experimental approach. Tectonics 19, 896–904. https://doi.org/10.1029/2000TC900015.

Minor, S.A., Hudson, M.R., Caine, J.S., Thompson, R.A., 2013. Oblique transfer of extensional strain between basins of the middle Rio Grande rift, New Mexico: fault

kinematic and paleostress constraints. In: Hudson, M.R., Grauch, V.J.S. (Eds.), New Perspectives on Rio Grande Rift Basins: from Tectonics to Groundwater. Geological Society of America Special Paper 494, pp. 345–382. https://doi.org/10.1130/2013.2494(14).
Mohr, P.A., 1970. The Afar Triple Junction and sea-floor spreading. J. Geophys. Res. 75, 7340–7352. https://doi.org/10.1029/JB075i035p07340.
Molnar, N.E., Cruden, A.R., Betts, P.G., 2017. Interactions between propagating rotational rifts and linear rheological heterogeneities: Insights from three-dimensional laboratory experiments. Tectonics 36, 420–443. https://doi.org/10.1002/2016TC004447.
Molnar, N.E., Cruden, A.R., Betts, P.G., 2018. Unzipping continents and the birth of micro-continents. Geology 46, 451–454. https://doi.org/10.1130/G40021.1.
Molnar, N.E., Cruden, A.R., Betts, P.G., 2019. Interactions between propagating rifts and linear weaknesses in the lower crust. Geosphere 15, 1–24. https://doi.org/10.1130/GES02119.1.
Mondy, L.S., Rey, P.F., Duclaux, G., Moresi, L., 2018. The role of asthenospheric flow during rift propagation and breakup. Geology 46, 103–106. https://doi.org/10.1130/G39674.1.
Morley, C.K., Nelson, R.A., Patton, T.L., Munn, S.G., 1990. Transfer Zones in the East African Rift System and Their Relevance to Hydrocarbon Exploration in Rifts. AAPG Bull. 74, 1234–1253. https://doi.org/10.1306/0C9B2475-1710-11D7-8645000102C1865D.
Müller, R.D., Gaia, C., Roest, W.R., Hansen, D.L., 2001. A recipe for microcontinent formation. Geology 29, 203–206. https://doi.org/10.1130/0091-7613(2001)029<0203:ARFMF>2.0.CO;2.
Mulugeta, G., 1988. Squeeze box in the centrifuge. Tectonophysics 148, 323–335. https://doi.org/10.1016/0040-1951(88)90139-4.
Nelson, R.A., Patton, T.L., Morley, C.K., 1992. Rift-Segment Interaction and Its Relation to Hydrocarbon Exploration in Continental Rift Systems. AAPG Bull. 76, 1153–1169. https://doi.org/10.1306/BDFF898E-1718-11D7-8645000102C1865D.
Nunns, A.G., 1982. The Structure and Evolution of the Jan Mayen Ridge and Surrounding Regions. In: Watkins, J.S., Drake, C.L. (Eds.), Studies in Continental Margin Geology, vol. 3. AAPG Memoir, pp. 193–208. https://doi.org/10.1306/M34430C10.
O'Bryan, J.W., Cohen, R., Gilliland, W.N., 1975. Experimental Origin of Transform Faults and Straight Spreading-Center Segments. GSA Bulletin 86, 793–796. https://doi.org/10.1130/0016-7606(1975)86<793:EOOTFA>2.0.CO;2.
Oldenburg, D.W., Brune, J.N., 1972. Ridge Transform Fault Spreading Pattern in Freezing Wax. Science 178, 301–304. https://doi.org/10.1126/science.178.4058.301.
Oldenburg, D.W., Brune, J.N., 1975. An explanation for the orthogonality of ocean ridges and transform faults. J. Geophys. Res. 80, 2575–2585. https://doi.org/10.1029/JB080i017p02575.
Panien, M., Schreurs, G., Pfiffner, A., 2006. Mechanical behaviour of granular materials used in analogue modelling: insights from grain characterisation, ring-shear tests and analogue experiments. J. Struct. Geol. 28, 1710–1724. https://doi.org/10.1016/j.jsg.2006.05.004.
Paul, D., Mitra, S., 2013. Experimental models of transfer zones in rift systems. AAPG Bull. 97, 759–780. https://doi.org/10.1306/10161212105.
Peron-Pinvidic, G., Gernignon, L., Gaina, C., Ball, P., 2012a. Insights from the Jan Mayen system in the Norwegian–Greenland Sea - I. Mapping of a microcontinent. Geophys. J. Int. 191, 385–412. https://doi.org/10.1111/j.1365-246X.2012.05639.x.
Peron-Pinvidic, G., Gernignon, L., Gaina, C., Ball, P., 2012b. Insights from the Jan Mayen system in the Norwegian–Greenland sea - II. Architecture of a microcontinent. Geophys. J. Int. 191, 413–435. https://doi.org/10.1111/j.1365-246X.2012.05623.x.
Philippon, M., Willingshofer, E., Sokoutis, D., Corti, G., Sani, F., Bonini, M., Cloetingh, S., 2015. Slip re-orientation in oblique rifts. Geology 43 (2), 147–150. https://doi.org/10.1130/G36208.1.
Purcell, P.G., 2017. Re-imagining and re-imaging the development of the East African Rift. Petrol. Geosci. 24, 21–40. https://doi.org/10.1144/petgeo2017-036.
Ramberg, H., 1981. Gravity, Deformation and the Earth's Crust. Academic Press, London.
Rosendahl, B.R., 1987. Architecture of Continental Rifts with Special Reference to East Africa. Annu. Rev. Earth Planet Sci. 15, 445–503. https://doi.org/10.1146/annurev.ea.15.050187.002305.
Rudolf, M., Boutelier, D., Rosenau, M., Schreurs, G., Oncken, O., 2016. Rheological benchmark of silicone oils used for analog modeling of short- and long-term lithospheric deformation. Tectonophysics 684, 12–22. http://dx.doi.org/10.1016/j.tecto.2015.11.028.
Saria, E., Calais, E., Stamps, D.S., Delvaux, D., Hartnady, C.J.H., 2014. Present-day kinematics of the East African Rift. J. Geophys. Res.: Solid Earth 119, 3584–3600. https://doi.org/10.1002/2013JB010901.
Schellart, W.P., Lister, G.S., Jessell, M.W., 2002. Analogue modelling of asymmetrical back-arc extension. In: Schellart, W.P., Passchier, C. (Eds.), Analogue Modelling of Large-Scale Tectonic Processes. Journal of the Virtual Explorer, vol. 7, pp. 25–42. https://doi.org/10.3809/jvirtex.2002.00046.
Schellart, W.P., Jessell, M.W., Lister, G.S., 2003. Asymmetric deformation in the backarc region of the Kuril arc, northwest Pacific: New insights from analogue modelling. Tectonics 22 (5), 1047. https://doi.org/10.1029/2002TC001473.
Schmid, T., Schreurs, G., Warsitzka, M., Rosenau, M., 2019. Effect of sieving height on density and friction of brittle analogue material: Ring-shear test data of quarz sand used for analogue experiments in the Tectonic Modelling Lab of the University of Bern. GFZ Data Services. https://doi.org/10.5880/fidgeo.2020.006.
Schillington, D.J., Scholz, C.A., Chindandali, P.R.N., Gaherty, J.B., Accardo, N.J., Onyango, E., Ebinger, C.J., Nyblade, A.A., 2020. Controls on Rift Faulting in the North Basin of the Malawi (Nyasa) Rift, East Africa. Tectonics 39, e2019TC005633. https://doi.org/10.1029/2019TC005633.
Sun, Z., Zhong, Z., Keep, M., Zhou, D., Cai, D., Li, X., Wu, S., Jiang, J., 2009. 3D analogue modelling of the South China Sea: A discussion on breakup pattern. J. Asian Earth Sci. 34, 544–556. https://doi.org/10.1016/j.jseaes.2008.09.002.
Talwani, M., Eldholm, O., 1977. Evolution of the Norwegian-Greenland Sea. GSA Bulletin 88, 969–999. https://doi.org/10.1130/0016-7606(1977)88<969:EOTNS>2.0.CO;2.
Tentler, T., Acocella, V., 2010. How does the initial configuration of oceanic ridge segments affect their interaction? Insights from analogue models. J. Geophys. Res. 115, B01401. https://doi.org/10.1029/2008JB006269.
Torsvik, T.H., Van der Voo, R., Preeden, U., Mac Niocaill, C., Steinberger, B., Doubrovine, P.V., Van Hinsbergen, D.J.J., Domeier, M., Gaina, C., Tohver, E., Meert, J.G., McCausland, P.J.A., Cocks, L.R.M., 2012. Phanerozoic polar wander, palaeogeography and dynamics. Earth Sci. Rev. 114, 325–368. https://doi.org/10.1016/j.earscirev.2012.06.007.
Trudgill, B., Cartwright, J., 1994. Relay-ramp forms and normal-fault linkages, Canyonlands National Park, Utah. GSA Bulletin 106, 1143–1157. https://doi.org/10.1130/0016-7606(1994)106<1143:RRFANF>2.3.CO;2.
Twiss, R.J., Moores, E.M., 1992. Structural Geology. W.H. Freeman and Company, New York.
Ustaszewski, K., Schumacher, M.E., Schmid, S.M., Nieuwland, D., 2005. Fault reactivation in brittle–viscous wrench systems–dynamically scaled analogue models and application to the Rhine–Bresse transfer zone. Quat. Sci. Rev. 24, 365–382. https://doi.org/10.1016/j.quascirev.2004.03.015.
Van der Pluim, B.A., Marshak, S., 2004. Earth Structure. W.W. Norton & Company Ltd., New York.
Van Wijk, J.W., 2005. Role of weak zone orientation in continental lithosphere extension. Geophys. Res. Lett. 32, L02303 https://doi.org/10.1029/2004GL022192.
Van Wijk, J.W., Blackman, D.K., 2005. Dynamics of continental rift propagation: the end-member modes. Earth Planet Sci. Lett. 229, 247–258. https://doi.org/10.1016/j.epsl.2004.10.039.
Weijermars, R., Schmeling, H., 1986. Scaling of Newtonian and non-Newtonian fluid dynamics without inertia for quantitative modelling of rock flow due to gravity (including the concept of rheological similarity). Phys. Earth Planet. In. 43, 316–330. https://doi.org/10.1016/0031-9201(86)90021-X.
Zwaan, F., Schreurs, G., Naliboff, J., Buiter, S.J.H., 2016. Insights into the effects of oblique extension on continental rift interaction from 3D analogue and numerical models. Tectonophysics 693, 239–260. https://doi.org/10.1016/j.tecto.2016.02.036.
Zwaan, F., Schreurs, G., 2017. How oblique extension and structural inheritance influence rift segment interaction: Insights from 4D analog models. Interpretation 5, SD119–SD138. https://doi.org/10.1190/INT-2016-0063.1.
Zwaan, F., Schreurs, G., Adam, J., 2018a. Effects of sedimentation on rift segment evolution and rift interaction in orthogonal and oblique extensional settings: Insights from analogue models analysed with 4D X-ray computed tomography and digital volume correlation techniques. Global Planet. Change 171, 110–133. https://doi.org/10.1016/j.gloplacha.2017.11.002.
Zwaan, F., Schreurs, G., Gentzmann, R., Warsitzka, M., Rosenau, M., 2018b. Ring-shear test data of quartz sand from the Tectonic Modelling Lab of the University of Bern (CH). V. 1. GFZ Data Services. https://doi.org/10.5880/fidgeo.2018.028.
Zwaan, F., Schreurs, G., Ritter, M., Santimano, T., Rosenau, M., 2018c. Rheology of PDMS-corundum sand mixtures from the Tectonic Modelling Lab of the University of Bern (CH). V. 1. GFZ Data Services. https://doi.org/10.5880/fidgeo.2018.023.
Zwaan, F., Schreurs, G., Buiter, S.J.H., 2019. A systematic comparison of experimental set-ups for modelling extensional tectonics. Solid Earth 10, 1063–1097. https://doi.org/10.5194/se-10-1063-2019.
Zwaan, F., Scheurs, G., Rosenau, M., 2020. Rift propagation in rotational versus orthogonal extension: Insights from 4D analogue models. J. Struct. Geol. 135, 103946 https://doi.org/10.1016/j.jsg.2019.103946.
Zwaan, F., Schreurs, G., 2020. 4D X-Ray CT data and surface view videos of analogue models exploring rift interaction in orthogonal and rotational extension. GFZ Data Services. https://doi.org/10.5880/fidgeo.2020.031.